iScience

CellPress
OPEN ACCESS

Article

Controlling basal plane sulfur vacancy in water splitting MoSx/NiF electrocatalysts through electric-field-assisted pulsed laser ablation

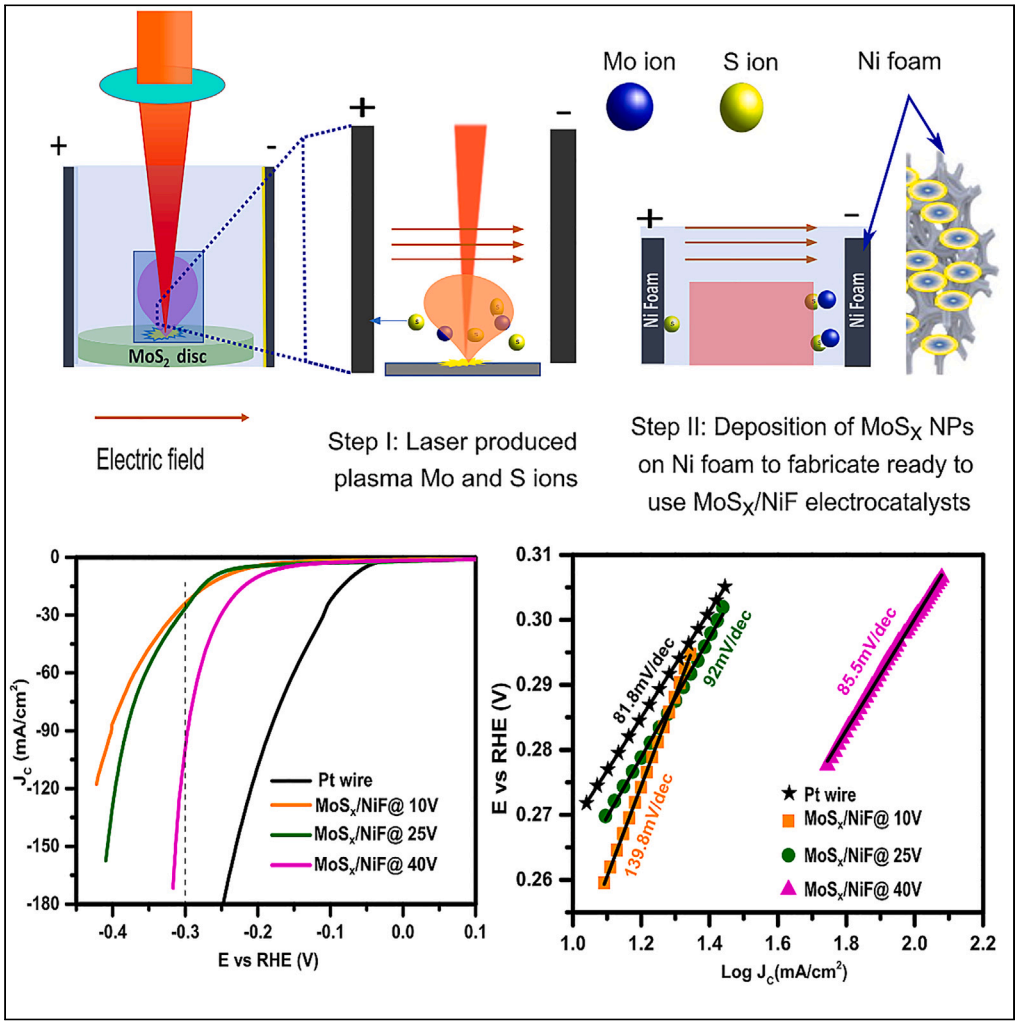

Chaudry Sajed Saraj, Subhash C. Singh, Roshan Ali, ..., Weili Yu, Wei Li, Chunlei Guo

ssingh49@ur.rocheester.edu (S.C.S.)
weili1@ciomp.ac.cn (W.L.)
guo@optics.rochester.edu (C.G.)

Highlights

EF-PLA fabricate ready-to-use electrocatalysts for overall water splitting

The applied electric-field parameters efficiently control S-vacancy

The experimental finding supported by DFT calculations

The obtained materials showed high activity toward overall water splitting

Saraj et al., iScience 26, 106797
June 16, 2023
https://doi.org/10.1016/j.isci.2023.106797

iScience

CellPress
OPEN ACCESS

Article

Controlling basal plane sulfur vacancy in water splitting MoSx/NiF electrocatalysts through electric-field-assisted pulsed laser ablation

Chaudry Sajed Saraj,[1,3] Subhash C. Singh,[2,*] Roshan Ali,[1,3] Abhishek Shukla,[1] Gopal Verma,[1] Ting Ting Zou,[1] Weili Yu,[1] Wei Li,[1,3,4,*] and Chunlei Guo[2,*]

SUMMARY

Eco-friendly, efficient, and durable electrocatalysts from earth-abundant materials are crucial for water splitting through hydrogen and oxygen generation. However, available methods to fabricate electrocatalysts are either hazardous and time-consuming or require expensive equipment, hindering the large-scale, eco-friendly production of artificial fuels. Here, we present a rapid, single-step method for producing MoS_x/NiF electrocatalysts with controlled sulfur-vacancies via electric-field-assisted pulsed laser ablation (EF-PLA) in liquid and *in-situ* deposition on nickel foam, enabling efficient water splitting. Electric-field parameters efficiently control S-vacancy active sites in electrocatalysts. Higher electric fields yield a MoS_x/NiF electrocatalyst with a larger density of S-vacancy sites, suited for HER due to lower Gibbs free energy for H* adsorption, while lower electric fields produce an electrocatalyst with lower S-vacancy sites, better suited for OER, as shown by both experimental and theoretical results. The present work opens a horizon in designing high-efficiency catalysts, for a wide range of chemical reactions.

INTRODUCTION

The continuous rise in global energy demand and the growing concern about climate change have kindled rapid research and development on renewable energy generation and storage.[1–4] Hydrogen is an ideal and sustainable fuel since it has a high energy density and clean combustion when it is burned. Electrocatalytic water splitting is an effective and environment-friendly method of producing clean hydrogen; however it requires highly active catalyst materials for the hydrogen evolution reaction (HER) and the oxygen evolution reaction (OER). These reactions are responsible for boosting the generation of hydrogen (H_2) and oxygen (O_2).[5–8] Platinum (Pt)-based materials and Ru/Ir oxides, due to their strong chemical and corrosion resistance and low overpotential, are best electrocatalys for HER and OER, respectively.[9–14] But, these electrocatalysts materials are not naturally abundant and expensive, which makes it hard to use them in industrial-scale production of hydrogen.[15–18] In addition, most of the known electrocatalysts are not suitable for both HER and OER activities in the same electrolyte medium due to their incompetency to activate and operate in a wide pH range.[19,20] Therefore, there have been increasing efforts in developing simple and facile ways to produce high-efficiency and low-cost bifunctional electrocatalysts from earth-abundant materials.[21–27]

Molybdenum disulfide (MoS_2) is an excellent non-noble metal electrocatalyst for HER due to active sulfur atoms and bandgap alignment with the hydrogen redox potential.[28–30] It is considered as a bifunctional electrocatalyst and a promising alternative to Pt and RuO_2 due to its earth abundance, relatively low cost, high catalytic activity, and excellent stability in acidic as well as alkaline media.[31–34] However, several studies found that only the edges of 2D MoS_2 flakes or the surfaces of MoS_2 nanostructures have active sulfur atoms, but most of the atoms in the volume or at the basal planes are inactive.[35,36] Significant research efforts have been invested to physically or chemically enhance the electrocatalytic efficiency of MoS_2 either through edge site engineering or by enhancing the intrinsic activity of edge sites through chemical doping.[37–40] The first strategy of edge site engineering is focused on increasing the edge/surface sites of MoS_2 through nano-structuring including the synthesis of smaller-sized nanoparticles, quantum dots, nanowires, nanoflakes, and defect-rich films.[37–39,41–44] However, the second strategy is to enhance the

[1]GPL Photonics Laboratory, State Key Laboratory of Luminescence and Applications, Changchun Institute of Optics, Fine Mechanics and Physics, Chinese Academy of Sciences, Changchun, Jilin 130033, P. R. China

[2]The Institute of Optics, University of Rochester, Rochester, NY 14627, USA

[3]University of Chinese Academy of Sciences (UCAS), Beijing 100049, China

[4]Lead contact

*Correspondence: ssingh49@ur.rocheester.edu (S.C.S.), weili1@ciomp.ac.cn (W.L.), guo@optics.rochester.edu (C.G.)

https://doi.org/10.1016/j.isci.2023.106797

intrinsic activity of edge/surface sites by modifying the bandgap using chemical doping or surface functionalization.[40,45–47]

Another strategy, potentially most effective but less explored, is by activating sulfur atoms on the basal plane of MoS_2, the majority of the inert materials in the bulk, to fully utilize most of the materials in the volume to enhance its electrocatalytic efficiency.[48,49] Therefore, a simple, efficient, and environment-friendly method for generating S-vacancy in the basal plane/volume of MoS_2 NPs is highly desirable. Very recently, there have been limited research efforts in activating S-vacancy sites at the basal plane of MoS_2 to enhance its electrocatalytic HER performance.[50–53] However, these studies either require costly equipment or multi-step time-consuming operations, which limit the application of S-deficient MoS_2 electrocatalysts.[50,51,53–55] For example, argon or hydrogen plasma post-processing treatments on chemical vapor deposition or molecular beam epitaxy-grown MoS_2 flakes were used to generate S-vacant MoS_2 electrocatalysts.[53,54] To realize industrial-scale water splitting, a facile, environmental-friendly, scalable, low-cost, and simple method is required to generate S-deficient MoS_2.

Here, we present an environmentally friendly, single-step, physical top-down technique of electric-field-assisted pulsed laser ablation (EF-PLA) of MoS_2 target (solid-disc) in water[56] for generation of S-deficient MoS_x NPs and their simultaneous dielectrophoretic deposition on nickel foam (NiF), to fabricate ready-to-use[8] electrocatalysts on support for overall water splitting. Although pulsed laser ablation in liquid (PLA) offers several benefits for synthesizing nanoparticles (NPs); however, their usefulness is typically restricted to solution-phase applications.[57–61] Specifically, when utilized for electrocatalytic purposes, it is typically necessary to separate the NPs from the solution via centrifugation, disperse them in a mixture of alcohol and Nafion, and redeposit them onto a glassy carbon electrode before conducting electrochemical measurements.[62] So, we are using an electric-field-assisted pulsed laser ablation (EF-PLA) method, that gives us a ready-made electrocatalysts that doesn't require any further processing. The applied external electric field across laser-produced plasma (LPP), containing Mo and S ions, forces S ions to migrate from the nucleation and growth region to produce S-deficient and positive surface charged MoS_x NPs. The as-produced positive surface charged MoS_x NPs gets di-electrophoretically deposited on the negatively biased NiF substrate to fabricate MoS_x/NiF electrocatalysts. The applied electric field effectively controls the S-active sites present in the electrocatalysts and, as a result, the HER and OER performances of the electrocatalysts. MoS_x/NiF electrocatalyst produced at higher electric field (40V/cm) has highest density of S-vacancy sites. Experimental and density functional theoretical (DFT) calculations have shown that a MoS_x/NiF electrocatalyst with a higher density of S-vacancy sites is better suited for HER due to a lower Gibbs free energy (ΔG_{H^*}) for H* adsorption. Therefore, MoS_x/NiF electrocatalyst produced at 40 V/cm electric field shows 150-mA/cm^2 cathodic current density at an overpotential of ~310 mV with the Tafel slope as low as 66 mV/dec. Conversely, a MoS_x/NiF electrocatalyst produced at a lower (10 V/cm) electric field exhibits a comparatively higher S/Mo ratio is found more suitable for the OER with the Tafel slope as low as 71 mV/dec. Importantly, when the highest S-vacant electrocatalyst and the lowest S-vacant electrocatalyst samples are assembled as cathode and anode, respectively to build a two-electrode cell, the cell requires only 1.63 V of potential to drive 10 mA/cm^2 of current density with an excellent stability. This work opens a horizon in designing of high-efficiency catalysts, beyond MoS_x, for a wide range, beyond HER and OER, of chemical reactions.

RESULTS AND DISCUSSION

Synthesis and structural characterizations of MoS_x/NiF electrocatalysts

Scheme 1 illustrates our novel top-down approach of EF-PLA synthesis of MoS_x NPs and their *in-situ* dielectrophoretic deposition on a high-purity Ni-foam (NF) conductive substrate. NF is selected as the substrate due to its multidimensional electron transport pathway and interconnecting porous networks. A pulsed laser beam irradiates surface of a MoS_2 target, submerged in water, at the solid-liquid interface to produce a high-temperature, high-pressure, and high-density laser-produced plasma (LPP) in the presence of an external electric field (Scheme 1A). The LPP contains Mo and S ions. In general, liquid confined LPP plume has a cluster formation zone, where species from the plasma plume assemble to make nuclei, and these nuclei grow with the consumption of ionic species from the plasma to generate NPs.[63–68] In the course of nucleation and growth, the ratio of S and Mo ions in MoS_x NPs can be controlled using the density and dynamics of positively (Mo^{4+}) and negatively (S^{2-}) charged species in the cluster formation zone of the LPP. The applied external electric field can force S ions, lighter ions of the plasma, to migrate from the LPP toward the positive electrode and the density of S ions that could be migrated depends on the

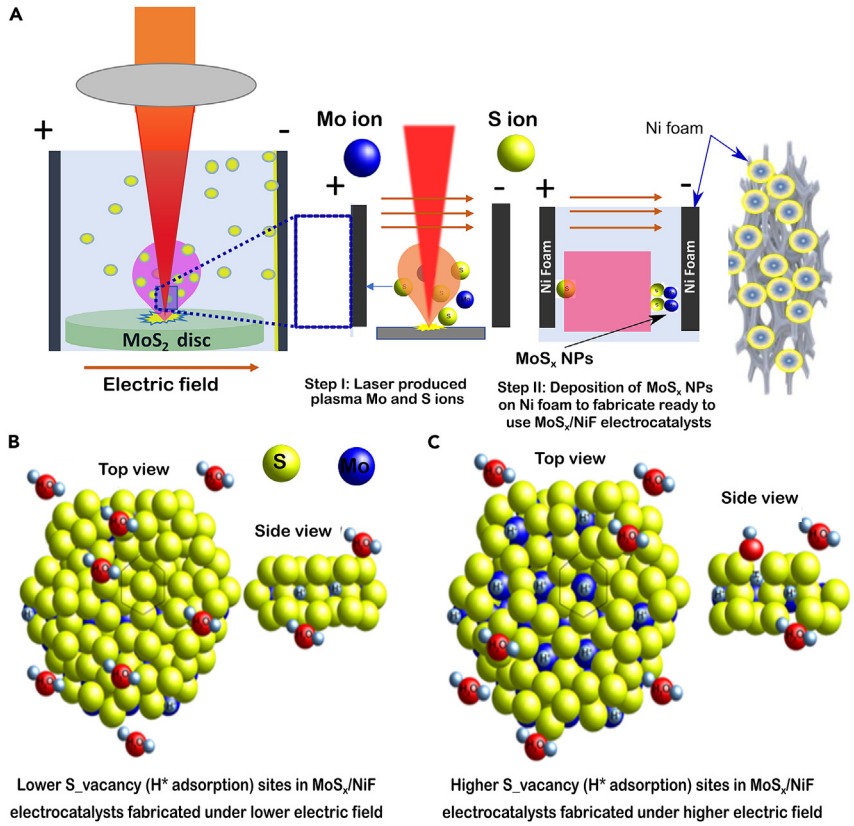

Scheme 1. Schematic illustrations of synthesis of MoS_x NPs and their in-situ dielectrophoretic deposition on a high-purity Ni foam conductive substrate

(A–C) (A) Electric field assisted pulsed laser ablation (EF-PLA) in water for the generation of sulfur-deficient MoS_x NPs and their simultaneous electrophoretic deposition on substrate. Step I: Migration of a few sulfur ions from the laser-produced plasma towards the positive electrode and step II: clustering of the rest of the cationic and anionic plasma species to generate positive surface charged MoS_x NPs and their di-electrophoretic deposition on the negatively biased substrate to make MoSx/NiF electrocatalysts. Sketches of MoS_x NPs with (B) higher x value (lower S-vacancy) in MoS_x NPs produced under lower electric field, and (C) lower x value (higher S-vacancy) under higher electric field. In (C) a greater number of Mo and S-vacancy sites are available for H* adsorption for the high HER performance.

magnitude of the applied electric field (Step I: Scheme 1A).[69–71] The remaining ionic species in the LPP could assemble to form positive surface charged MoS_x^{n+} NPs, where the values of x (S/Mo ratio) and surface charge (n) depend on the rate of the S ions migration from the LPP. This rate depends on magnitude of the applied electric field. The as-produced positive surface charged and S-deficient MoS_x^{n+} NPs can get dielectrophoretically deposited on the negatively biased Ni foam to fabricate a ready-to-use MoS_x/NiF electrocatalysts (Step II: Scheme 1A).[72,73] The S-vacant sites in the MoS_x NPs unveil Mo sites having comparatively lower Gibbs free energy (ΔG_H) for the H* adsorption.[52] The higher applied electric field can produce a higher density of S-vacancy sites and unveil a larger number of Mo atoms for a higher density of H* adsorption in HER and vice versa (Schemes 1B and 1C).

The normalized UV-visible absorption spectra of the colloidal solution of MoS_x NPs generated at different magnitudes of the applied electric field are shown in Figure 1A (see Figures S1A and S1B). A strong absorption peak observed at ~235 nm can be assigned as the blue-shifted convolution of C, D, and Z excitonic peaks of MoS_2 NPs/QDs[74–76] and can be considered as a characteristic absorption peak of MoS_2 NPs/QDs.[77] The blue shift (see Figures S1B–S1D) in the characteristic absorption peak at a higher electric field demonstrates the formation of smaller size particles (see STAR Methods section and Figure S1D).[78–80] The decrease in the size of NPs with an increase in the applied field may be associated with the quicker electric-field-induced transfer of the growing NPs from the growth zone to the bulk solution.

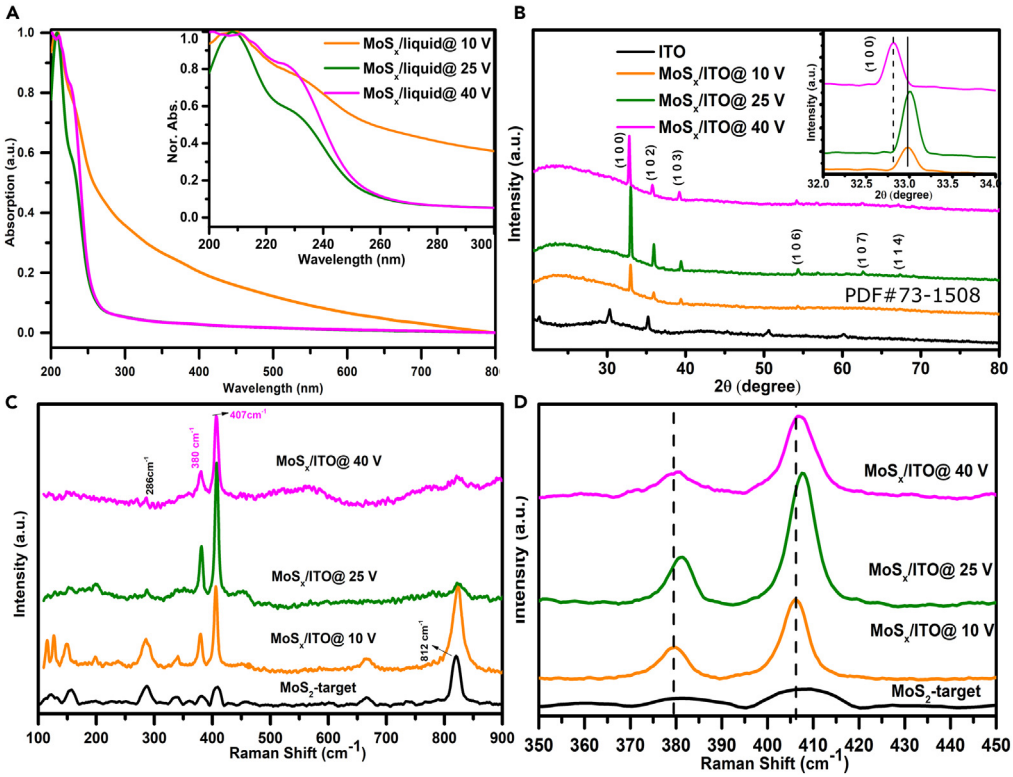

Figure 1. Optical, structural, and compositional characterizations of MoS_x NPs

(A) The UV-visible absorption spectra of MoS_x NPs produced in the solution under different electric fields.

(B–D) The inset shows an enlarged view, (B) the XRD spectra of MoS_x NPs deposited on ITO-coated glass slides under different electric fields. The Raman spectra of MoS_x NPs electrophoretically deposited on ITO-coated glass slide and Solid MoS_2 target in the frequency range of (C) 100–900 cm^{-1} and (D) an enlarged view in 350–450 cm^{-1}.

For the X-ray diffraction (XRD) measurements, two ITO-coated glass electrodes were used instead of Ni foam, and a similar procedure was followed to deposit corresponding MoS_x NPs on the substrate. The XRD results of MoS_x NPs deposited on negatively biased ITO-coated electrodes are shown in Figure 1B. A strong diffraction peak observed at $2\theta = 32.8°$ (PDF# 73–1508) corresponding to the reflection from (100) plane, with an interlayer (d) spacing of 0.272 nm, indicating preferential growth of a typical lamellar structure along the c axis. The 15 to 20 times lower intensities of all the other diffraction peaks, observed at wider angles, over the (100) peak shows quasi-monocrystalline nature of the as-produced MoS_x NPs (see Figure S2A and S2B). The intensity of a diffraction peak from a lattice plane is a result of the constructive interference of X-ray photons diffracting from different layers of that plane. Therefore, a decrease in the intensity of diffraction peak and increase in its FWHM exhibit synthesis of smaller-sized QDs with a fewer number of layers (see Figures S2A and S2B). The crystallite size of the MoS_x NPs, estimated from the Scherrer's formula, produced at 10, 25, and 40 V/cm of external electric fields are ~8, 69, and 66 nm, respectively (see Figure S2B). As we have two parallel electrodes, the NPs are depositing on both the electrodes. Therefore, for comparasion, we also performed XRD measurements of MoS_x NPs deposited on the positively biased ITO-coated electrode at an electric field of 10 V/cm. Interestingly, we observed that the crystalline nature of the MoS_x NPs at different electrodes are quite different (see Figure S3). Unlike the c-axis grown NPs on the negative electrode, the XRD of NPs deposited on the positive electrodes shows reflection characteristics (002) peak at $2\theta = 14.50°$ of few-layer MoS_2. The Raman spectroscopy is a common, simple, and highly reliable tool to investigate crystal structure of nanocrystals. Figures 1C and 1D show the Raman spectra of the bulk MoS_2 target used in the laser ablation and EF-PLA produced MoS_x NPs under different applied electric fields. The Raman scattering peaks observed at ~287, ~382, and ~407 cm^{-1} are characteristic, E^1_g, E^1_{2g}, and A_{1g} vibrational modes of hexagonal 2H MoS_2. As compared to the bulk MoS_2, the Raman spectra of the samples produced with EF-PLA show a blue shift in the Raman vibrational modes with ~25 cm^{-1} separation (Δk) between E^1_{2g}, and A_{1g} vibrational modes and enhancement in the relative

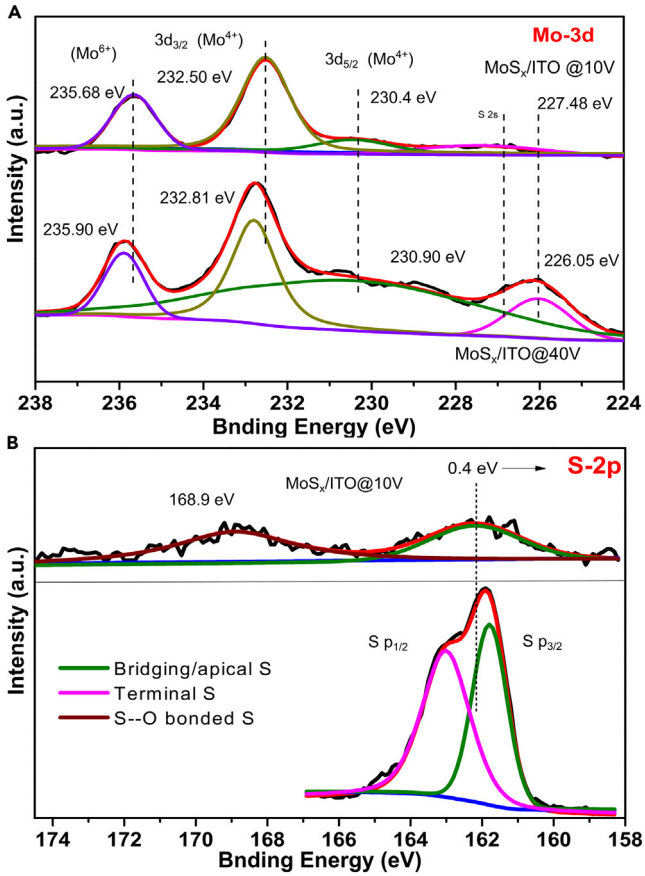

Figure 2. The XPS spectra of EF-PLA-fabricated MoS_x/NiF electrocatalysts

(A and B) (A) Mo 3days and (B) S 2p peaks for MoS_x/NiF@40 (bottom row), and MoS_x/NiF@10 (top row).

intensity. The observed blue shift can be attributed to an increase in the surface strain due to nanoparticle formation while relative increase in the Raman intensity can be associated with an increase in out-of-plane motion of the sulfur atoms. Decrease in the Raman intensity for the MoSx/ITO@40V sample compared to MoSx/ITO@25 shows increase in the S-vacancy sites. The decrease in the value of Δk for sample produced at the higher electric field indicates, and supports the XRD results, decrease in the number of layers grown in the c direction of the MoS_x NPs. To prove that the application of an external electric field during EF-PLA can control S-vacancy in the MoS_x NPs, we performed X-ray photoelectron spectroscopy (XPS) measurements to investigate the chemical composition of as-produced MoS_x electrocatalysts (see supplemental information Figure S4). Since XPS is a surface sensitive technique, therefore roughness of NiF may affect XPS results of MoSx NPs. To avoid this issue, we electrophoretically deposited MoSx NPs on ITO-coated glass substrates. A high-resolution XPS spectra of Mo3d (Figure 2A) and S2p (Figure 2B) species from the MoS_x electrocatalysts fabricated under 40 V/cm (MoS_x@40; lower panel) and 10 V/cm (MoS_x@10; upper panel) of applied electric fields are shown in Figures 2 and S4. A doublet peak of Mo 3d at 229 and 232.3 eVs, which can be attributed to the Mo $3d_{5/2}$ and Mo $3d_{3/2}$ lines, respectively, of the Mo^{4+} oxidation state of MoS_2, is seen in the XPS spectra of both the samples. Since Mo ions of LPP are oxidized by O or OH ions of the plasma-induced plasma (PIP) produced at the LPP-water interface, an additional peak appears at 235.4 eV corresponding to the Mo^{6+} oxidation state, indicating the presence of MoO_3. This has been reported for a number of metal-liquid combinations.[64] The photoelectron peak observed at ~226.4 eV corresponds to the sulfur 2s state. The populations of Mo^{6+} and Mo^{4+} valence states were 27 and 73% respectively in the MoSx@10V electrocatalyst sample. The corresponding S2p spectra (Figure 2B) were deconvoluted into two peaks centered at ~162.8 eV. The S2p peak at the lower electron binding energy can be assigned to the bridging and/or apical sulfur, while the one with higher electron-binding energy can be associated with the terminal/unsaturated sulfur atoms. An

Table 1. Summary of XPS data for as-prepared MoS_x samples

MoSx/ITO samples	Mo^{4+}	Mo^{6+}	$S_{bridg.}$	$S_{term.}$	S_{S-O}
MoS_2/ITO@10V	230.41/232.5	235.7	162.2	-	168.9
MoS_2/ITO@40V	230.9/232.81	235.9	161.8	163	-
	$S_{term}/S_{bridg.}$	S-O/S_{total}	Mo^{4+}/Mo^{6+}	S_{total}/Mo^{4+}	Comp.
MoS_2/ITO@10V	–	0.64	2.71 (Mo^{4+}: 73%, Mo^{6+}:27%)	1.77	$MoS_{1.77}$
MoS_2/ITO@40V	1.25	–	5.28 (Mo^{4+}: 84%, Mo^{6+}:16%)	0.36	$MoS_{0.36}$

additional XPS peak centered at ~168.6 eV can be assigned to the -S-O bond associated with the oxidation of sulfur atoms.

From these XPS data, we can see that $3d_{3/2}$ (~232.3 eV) peak of Mo^{4+} and 3d (~235.4 eV) peak of Mo^{6+} get shifted toward the higher energy side, while $3d_{5/2}$ (~229 eV) peak get shifted toward the lower energy side in the samples produced at the higher applied electric field. Similarly, XPS peaks corresponding to $S2p_{3/2,}$ $S2p_{1/2,}$ and S-O are shifted to the lower energy values in the electrocatalysts produced at higher electric field. As can be seen from Table 1, the populations of Mo^{4+} (Mo^{6+}) are 73% (27%), and 84% (16%) in the MoS_x/NiF@10, and MoS_x/NiF@40 electrocatalysts, respectively. The percentage of oxidized sulfur atoms (S-O bonds) gets increased, while the ratio of terminal S to bridging S (S_{term}/S_{bridg}) gets decreased with an increase in the applied electric field. From the XPS investigations, we can conclude that the S-vacancy in as-produced MoS_x samples increased while the oxidation of Mo (i.e., the population of Mo^{6+} and consequently the synthesis of Mo_2O_3) is decreased in the electrocatalysts fabricated at the higher electric field. The S_{total} to Mo^{4+} ratios are 1.77 and 0.36 resulting the formation of $MoS_{1.77}$/NiF and $MoS_{0.36}$/NiF electrocatalysts at 10, and 40 V/cm of applied electric fields, respectively. It has been reported previously that an increase in the percentage of S-vacancy sites in MoS_2 decreases the electronic bandgap energy and ΔG_{H^*} resulting an increase in the HER performance.[16,17] Additionally, the increase in the S-O signal intensity, i.e., increase in the interface of sulfide and oxide can further increase the electrocatalytic performance of MoS_x electrocatalysts.[81] The compositional information of the MoS_x samples, extracted from the corresponding XPS spectrum, is summarized in Table 1.

Figures 3, S5, and S6 show the scanning electron microscopy (SEM) images of different EF-PLA-fabricated MoS_x/NiF electrocatalysts. It is clear from these images that the NPs are uniformly deposited on the porous 3D skeleton of the Ni foam (see Figures S5 and S6 for details). Lower resolution SEM images (First row of Figures 3A–3D) reveal a layer-by-layer deposition of NPs on the Ni foam, with a somewhat higher rate of deposition near the edges owing to stronger electric fields (see the second column of Figure S5C). As discussed on the previous pages, the NPs produced at a higher electric field are smaller in size with narrower size distribution; therefore corresponding electrophoretically deposited film has substantially reduced fractures and higher packing density (right panel of Figures S5A–S5C). Compositional data obtained from EDS spectra (see Figure S7) are similar to those obtained from XPS studies, with S/Mo ratios of 1.11 and 0.48 in the MoS_x@40 and MoS_x@10 electrocatalyst samples, respectively.

Figures 3E–3H show transmission electron microscope (TEM) images (second row of Figure 3) and corresponding size distribution (third row of Figure 3) of as-synthesized MoS_x NPs. The NPs produced at a lower (25V/cm) electric field has a larger average size (48.5 nm) and a wider size distribution (33.1) over the NPs (average size; 12.4 nm: distribution; 11.8 nm) produced at a larger electric field (See Figures 3G and 3H). We performed high-resolution TEM (HR-TEM) measurements for the NPs produced at 40V/cm of applied electric field (Figures 3I–3K). Figure 3 (i) shows that the NPs have a crystalline core and a quasi-crystalline shell. A higher magnification imaging of the quasi-crystalline shell layer (Figures 3J and 3K) shows presence of 5–7 nm crystals in an amorphous matrix. Analyzing lattice fringes (Figure 3K) of these nanocrystals shows interplanar spacings of 0.229, 0.250, and 0.272 nm corresponding to (103), (102), and (100) planes of MoS_2 NPs.

HER performance of MoS_x/NiF electrocatalysts

A three-electrode configuration with an alkaline (1M KOH) electrolyte medium was used to measure the electrocatalytic HER performance of various as-prepared MoS_x/NiF electrocatalysts.

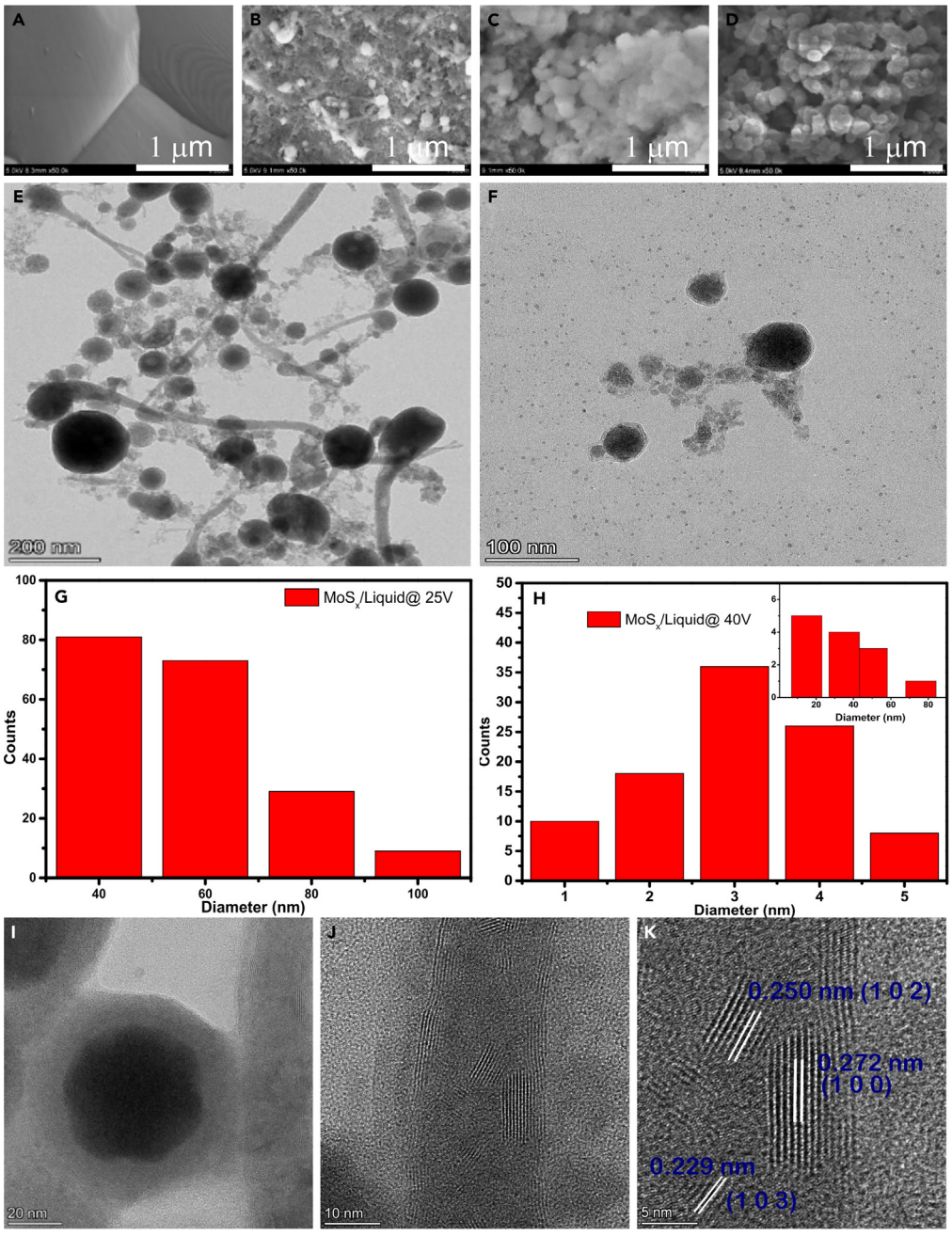

Figure 3. Structure and surface morphology characterizations of MoS_x/NiF electrocatalysts

(A–D) The SEM images of different as-fabricated electrocatalysts (A) Bare NiF (B)MoS_x/NiF@10, (C) MoS_x/NiF@25, and (D) MoS_x/NiF@40 electrocatalysts (Scale bar 1 mm).

(E–K) (E and F) TEM images and (G and H) corresponding size distribution of (E and F) MoS_x/NiF@25, and (F and H) MoS_x/NiF@40 NPs, (I–K) HR-TEM image of MoS_x/NiF@40 NPs.

These electrocatalysts had not undergo any post-processing treatment, loading, or adhesive coating. Figure 4A depicts the iR-compensated linear sweep voltammetry (LSV) curves of different MoS_x/NiF electrocatalysts with the LSV curve of Pt wire for comparison (see non-iR-compensated LSV curves in Figure S8). At a given overpotential, the MoS_x/NiF@40 electrocatalyst shows the maximum current density; therefore it is the best performer among the three samples. For example: At an overpotential of 300 mV (see vertical dashed line in Figure 4A), the current density (100 mA/cm^2) for MoS_x/NiF@40 sample is about 4 times

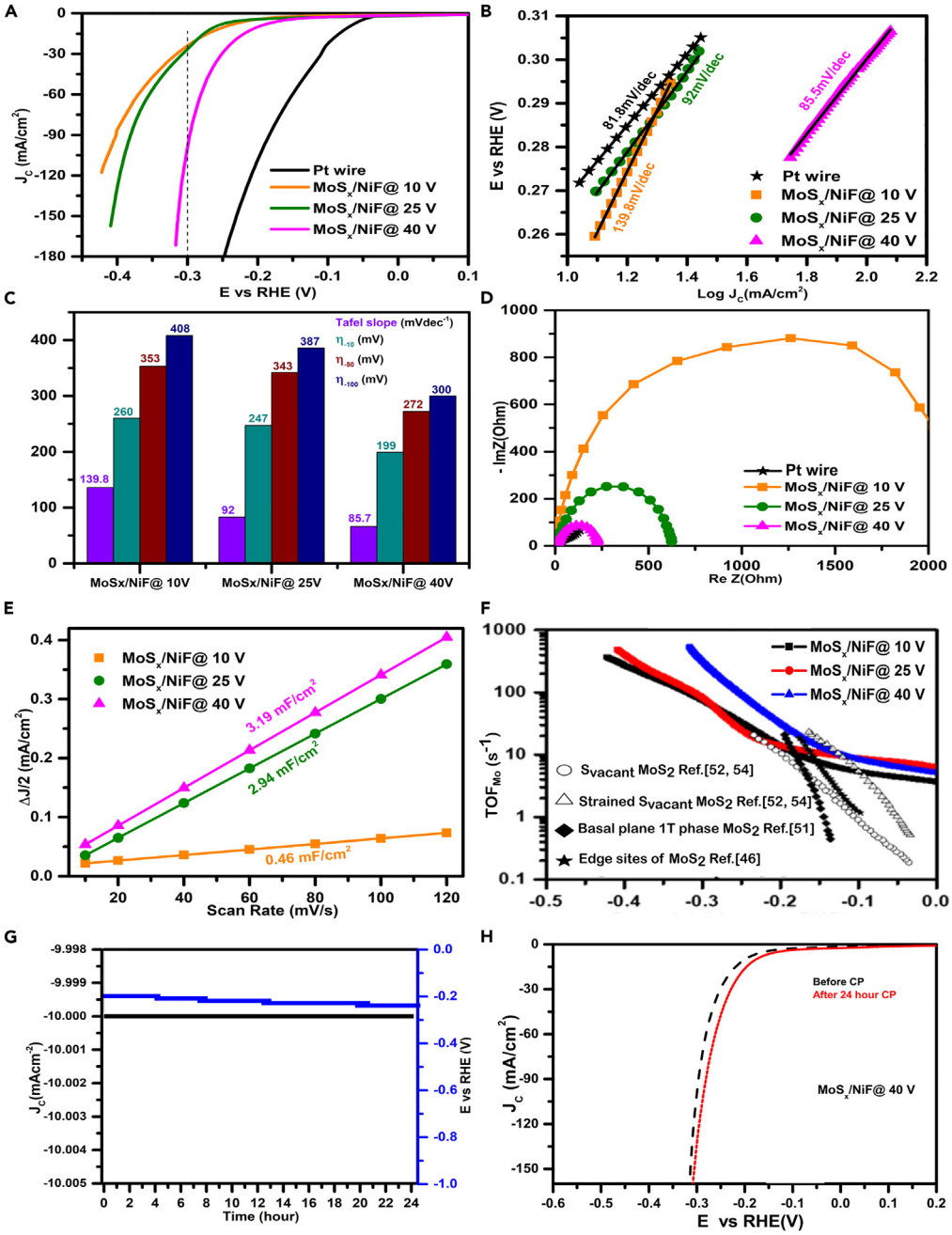

Figure 4. HER performance of different MoS_x/NiF electrocatalysts and Pt wire electrode

(A–D) (A) LSV curves, (B) Tafel slopes, (C) histograms for the Tafel slope and overpotentials (mV) for 10, 50, and 100 mA/cm^2 current densities, (D) corresponding Nyquist plots.

(E) Estimation of double-layer capacitance (C_{dl}) by plotting the mean of difference in cathodic and anodic currents with the scan rate.

(F–H) (F) Turnover frequencies for Mo sites (TOF_{Mo}) (G) Chronopotentiometry (CP) curve at 10 mA/cm^2 current density for 24 h, and (H) LSV curves before (dotted black) and after (solid red) 24 h of the CP measurement.

higher than the MoS_x/NiF@25 (~26 mA/cm^2) and MoS_x/NiF@10 (~24 mA/cm^2) electrocatalyst samples. The overpotential (η_{10}) for 10 mA/cm^2 of current density is much lower for the MoS_x/NiF@40 (199 mV) sample than the MoS_x/NiF@25 (247 mV) and MoS_x/NiF@10 (260 mV) electrocatalyst samples. Similarly, the η_{50}

(272 mV) and η_{100} (300 mV) overpotential values for MoS_x/NiF@40 sample are significantly lower than the samples MoS_x/NiF@25 (η_{50}: 343 mV and η_{100}: 387 mV) and MoS_x/NiF@10 (η_{50}: 353 mV and η_{100}: 408 mV) produced at the lower electric fields. The HER performance of our MoS_x/NiF electrocatalysts are tabulated with previously reported MoS_2-based HER electrocatalysts for comparison (Tables S1, S2, and S4).

Tafel slopes, obtained from the corresponding LSV curves, for the MoS_x/NiF@10, MoS_x/NiF@25, and MoS_x/NiF@40 samples are 140, 92, and 66 mV/dec, respectively (Figure 4B). We hypothesize that the higher reaction rate and faster HER kinetics in the MoS_x/NiF@40 electrocatalyst are a synergistic effect of the higher density of sulfur vacancy sites and the larger area of the sulfur-oxygen interface. From Figure 4C and Table S2 present the Tafel slopes and the various overpotential values for the three EF-PLA generated electrocatalyst samples. The EIS measurements of the electrocatalyst samples (Figure 4D) reveal that MoS_x/NiF@40 has a much lower charge-transfer resistance compared to MoS_x/NiF@25 and MoS_x/NiF@10 samples, leading to a faster rate of electron transfer from the electrocatalyst material for the reduction of surface-adsorbed H* in the Volmer step of HER. The electrochemical active surface area (ECSA) for each sample was calculated from the non-Faradaic section of the cyclic voltammetry (CV) curves recorded at varying scan rates to better understand the intrinsic activity of the electrocatalysts (see Figure S9). The MoS_x/NiF@40 exhibits the largest C_{dl} value (3.19 mF/cm^2) as compared to MoS_x/NiF@25 (2.94 mF/cm^2) and MoS_x/NiF@10 (0.46 mF/cm^2) (Figure 4E) electrocatalysts indicating larger ECSA value for MoS_x/NiF@40 (~1.5 cm^2) as compared to MoS_x/NiF@25 (~1.3 cm^2) and MoS_x/NiF@10 (~0.2 cm^2) samples (see supplemental information Table S2).

We further calculated the turnover frequency per surface Mo atoms (TOF_{Mo}) to compare the intrinsic activity of Mo among different MoS_x/NiF electrocatalysts (see STAR Methods for details) fabricated in this work. The TOF_{Mo} of our MoS_x/NiF electrocatalysts were compared with those reported previously.[52,82,83] As can be seen from Figure 4F, the intrinsic activity of Mo atoms at a given potential (>0.15 V versus RHE) is highest for the MoS_x/NiF@40 electrocatalyst, while it is the lowest for MoS_x/NiF@10. The difference between the intrinsic activities of Mo atoms in MoS_x/NiF@40 and MoS_x/NiF@25 or MoS_x/NiF@10 samples is larger at the higher overpotential. An increase in the density of S-vacancy sites in the MoSx/NiF samples increases the intrinsic HER activity of Mo sites. As reported previously, the TOF_{Mo} value for S-vacant MoS_2 was even higher than those of the basal plane of 1-T MoS_2 and MoS_2 edge sites indicating that the Mo sites in an S-vacant MoS_x are more HER active than the Mo sites in an stoichiometric MoS_2.[52] At lower overpotentials (<150 mV), the TOF_{Mo} values of all the three MoSx/NiF electrocatalysts are higher than the corresponding TOF values of unstrained S-vacant MoS_2 and strained S-vacant MoS_2 electrocatalysts,[52] 1T-phase MoS_2 basal plane[82] and MoS_2 edge sites[83] (see Figure S11). Similarly, we calculated the turnover frequency per S-vacant site ($TOF_{S\text{-}vacancy}$) (see STAR Methods section and Figure S10) to compare the intrinsic HER activity of S-vacancy sites and understanding its dependence on the S-vacancy density. The $TOF_{S\text{-}vacancy}$ follows the same trend as the TOF_{Mo} where the intrinsic activity of S-vacancy site increases with its density. For example, MoS_x/NiF@40 sample has the maximum density of S-vacancy ($MoS_{0.22}$) sites and the highest value of $TOF_{S\text{-}vacancy}$. Like the TOF_{Mo}, the difference in the $TOF_{S\text{-}vacancy}$ values between the MoSx/NiF@40 and MoSx/NiF@25 samples increases with the overpotential, indicating that the S-vacancy sites are playing a key role in the hydrogen generation at the larger overpotential values.

Stability of electrocatalysts is a crucial performance indicator for gauging their electrochemical capabilities. Figure 4G shows that nearly constant overpotential of ~200 mV (<5% fluctuation) is required to maintain a current density at 10 mA/cm^2 for 24 h when using a MoS_x/NiF@40 sample as a working electrode. Furthermore, after 24 h of the chronopotentiometry, there is no discernible change in the LSV curve of the MoSx/NiF@40 sample from the initially LSV recorded curve (Figure 4H). These studies insure stability and durability of the MoS_x/NiF@40 electrocatalyst in an alkaline environment.

OER performance of MoSx/NiF electrocatalysts

In the same alkaline (1 M KOH) electrolyte medium, the electrocatalytic OER performances of various as-prepared MoS_x/NiF electrocatalysts were studied. With iR compensation, the LSV curves in Figure 5A (see Figure S12) reveal that the density of S vacancies in the MoS_x/NiF electrocatalysts has a major impact on the OER kinetics. The η_{100} overpotential is the lowest for MoS_x/NiF@10 (1.60 V) sample as compared to MoS_x/NiF@25 (1.63 V) and MoS_x/NiF@40 (1.64 V) electrocatalysts, as shown by the LSV curves (Figure 5A). MoS_x/NiF@10 (1.635 V) electrocatalyst has the lowest η_{200} value compared to

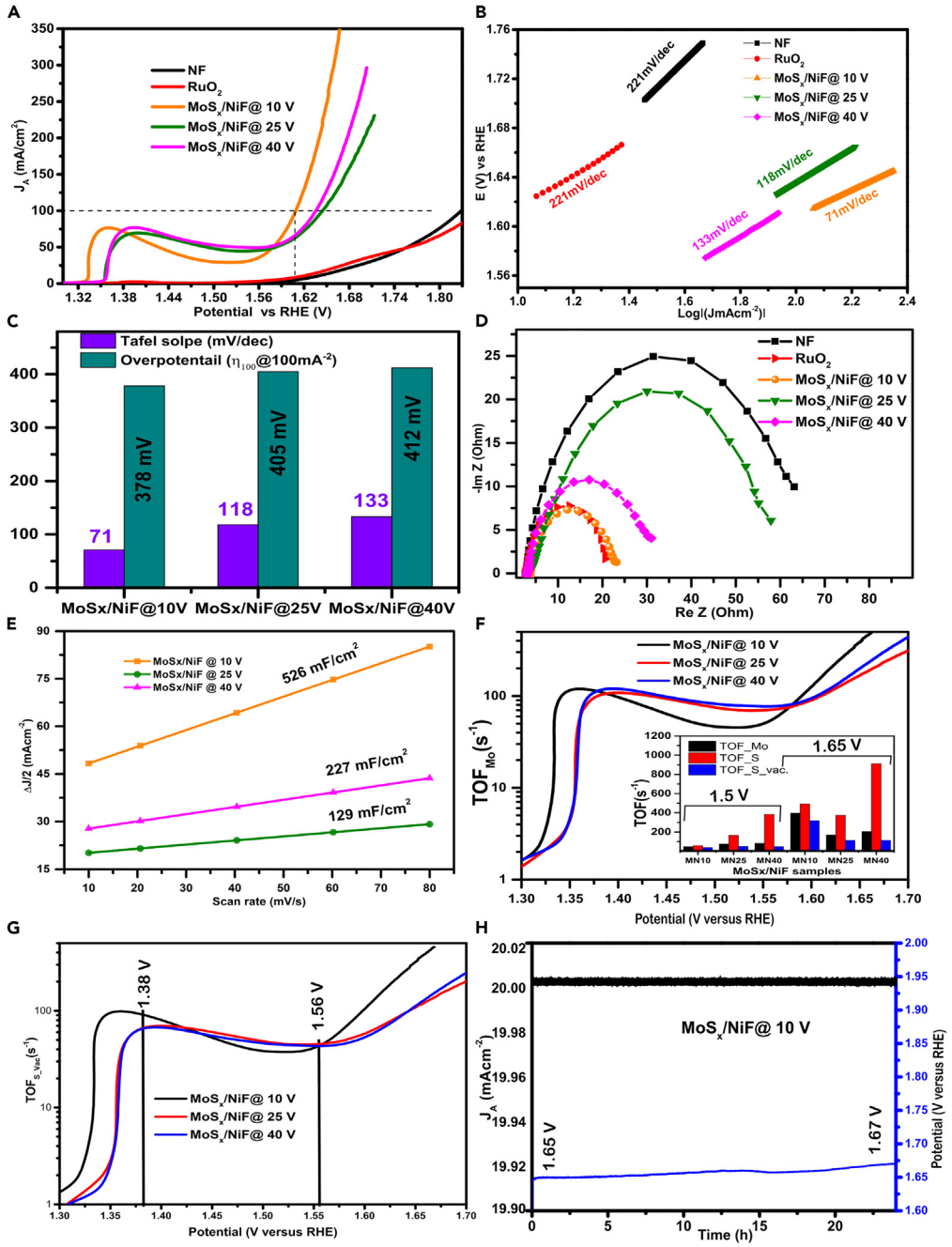

Figure 5. OER performance of MoS_{2-x} NPs electrophoretically deposited on Ni foam under different voltages and RuO_2 for comparison

(A–D) (A) LSV curves, (B) corresponding Tafel slope, (C) Tafel slope and overpotentials (mV) at 10 mA/cm^2 current density for different samples, (D) corresponding Nyquist plots.

(E–H) (E) Estimation of double-layer capacitance (C_{dl}) by plotting the mean of difference in cathodic and anodic currents with the scan rate. The corresponding turnover frequencies (F) at Mo sites: TOF_{Mo} and (G) S_vacancy sites: $TOF_{S\_vacancy}$, and (H) Long-term durability in the form of chronoamperometry of MoS_{2-x} NPs @ −10 V on Ni foam.

MoS_x/NiF@25 (1.67 V) and MoS_x/NiF@40 (1.7 V). Similarly, MoS_x/NiF@10 required the smallest value of potential (1.66 V) to reach a current density of 350 mA/cm^2. Similarly, the OER performance of our MoS_x/NiF electrocatalysts is tabulated with previously reported MoS_2-based OER electrocatalysts for comparison (Tables S3 and S5).

Calculated Tafel slopes for MoSx/NiF@10, MoSx/NiF@25, and MoSx/NiF@40 electrocatalysts are 71, 118, and 133 mV/dec, respectively; these values are smaller than the Tafel slopes for the bare Ni foam (221 mV/dec) and RuO_2 (221 mV/dec), as shown in Figure 5B. The Tafel slopes and overpotential values for different MoS_x/NiF electrocatalysts are presented in Figure 5C and summarized in supplemental information Table S3. From these results, surprisingly we can see that unlike the HER, where the electrocatalyst with the highest density of S-vacancy sites (MoS_x/NiF@40) was the best performer, in the OER, the electrocatalyst with the least density of S-vacancy sites (MoS_x/NiF@10) has the highest efficiency. Based on the EIS results, the rate of charge transfer at the electrode-adsorbate interface for the oxidation of intermediates (OH*, OOH*, O*) on the electrocatalyst surface is significantly higher for the MoS_x/NiF@10 sample than for the MoS_x/NiF@25 and MoS_x/NiF@40 samples (Figure 5D).

We computed ECSA values by extrapolating comparable C_{dl} values from the corresponding CV curves acquired in the non-Faradaic zone (1.23–1.53 V) at various scan rates in order to further investigate the intrinsic activity of various electrocatalysts against OER (see Figures S13–S14). Compared to MoS_x/NiF@25 (227 mF/cm^2) and MoS_x/NiF@40 (129 mF/cm^2), the C_{dl} value of the MoS_x/NiF@10 electrocatalyst has the highest (526 mF/cm^2) value (see Figures 5E, S13, and S14), therefore MoS_x/NiF@10 (50.8 cm^2) should have the largest ECSA value (see supplemental information Table S3). We further calculated the turnover frequencies of different active sites, TOF_{Mo}, TOF_S, and $TOF_{S\_Vacancy,}$ to compare their intrinsic OER activities in different MoSx/NiF electrocatalysts (see STAR Methods for details). As can be seen from Figures 5F and 5G, the intrinsic OER activities of each Mo and S-vacancy sites on the surface of MoS_x/NiF@10 sample is significantly higher than the corresponding activities of Mo and S atoms in MoS_x/NiF@25 and MoS_x/NiF@40 electrocatalysts. However, the intrinsic activity of S atoms is higher in the sample (MoS_x/NiF@40) due to larger density of S-vacancy sites (See Figure S15 and S16). The long-term durability of MoS_x/NiF@10 sample, tested for 24 h CP test at ~20 mA/cm^2 (Figure 5H; see Figure S17), shows <1.25% change in the initially required potential indicating excellent durability of the OER electrocatalyst in the alkaline medium.

Water splitting performance of MoS_x/NiF electrocatalysts

We built a two-electrode electrochemical cell with MoS_x/NiF@40 electrocatalyst at the cathode and MoS_x/NiF@10 electrocatalyst at the anode for overall water splitting based on the experimental HER and OER results, where MoS_x/NiF@40 and MoS_x/NiF@10 showed the highest HER and OER catalytic efficiency in the alkaline medium. As illustrated in Figure 6A with the circuit design in the inset, the cell was connected to a variable power source, a voltmeter, and an ammeter. An enlarged view of the two-electrode electrochemical cell is shown in the right panel of Figure 6A. First, the potential across the electrodes of the electrochemical cell was varied and the resulting current was measured. Figure 6B shows that a potential difference of 1.63 V is needed between electrodes to provide a current density of 10 mA/cm^2. In order to determine the stability of the MoS_x/NiF@40 MoS_x/NiF@10 electrochemical cell, we subjected it to a continuous voltage of 1.63 V and monitored the current density for 24 min. Figure 6C demonstrates the good endurance of the HER and OER electrocatalysts for water splitting in an alkaline medium, as the potential needed to drive 10 mA/cm^2 of the current density is kept close to 1.63 V Video S1 in the supplemental information demonstrate the kinetics of gas evolution at the cathode and the anode. Images of these films acquired at 1 s intervals are shown in Figures 6D and 6E for the hydrogen and oxygen evolutions, respectively.

Theoretical calculation analysis to understand mechanisms for HER and OER

To get a deeper understanding of the roles of S-vacancy sites on the intrinsic HER and OER catalytic activities of MoS_x/NiF electrocatalysts, the Gibbs free energies for H* (ΔG_{H^*}) and OH* (ΔG_{OH^*}) adsorption on stochiometric (MoS_2) and S-vacant MoS_x; x < 2) electrocatalysts were calculated using density functional theory (DFT) calculation method. We modeled monolayer of pure (0% S-vacant) 2H-MoS_2, and MoS_2 with different densities of S vacancies (18.7% and 25%) and different levels of oxygen atoms (Figure 7A). The ΔG_{H^*} values for H* adsorption on the surface of stochiometric and S-vacant MoS_2 (100) were calculated. As can be seen from Figure 7B, the ΔG_{H^*} value for the stochiometric MoS_2 is 1.97 eV and it decreased to 1.01 eV for the MoS_2 with 18.7% S-vacancy and 18.7% replacement of S atoms with O atoms. From these results, we can see that an increase in the S-vacancy, up to a certain level, can result $\Delta G_{H^*} = 0$, an ideal case for hydrogen generation. However, further increase in the S-vacancy, beyond a level where $\Delta G_{H^*} = 0$, increases ΔG_{H^*} value in the negative direction. For example: $\Delta G_{H^*} = -0.5$ eV for 25% of S-vacancy. From these DFT results, we can say that the higher HER efficiency of MoS_x/NiF@40 electrocatalyst sample over MoS_x/NiF@25 and MoS_x/NiF@10 electrocatalyst is due to the lower Gibbs energy for hydrogen adsorption.

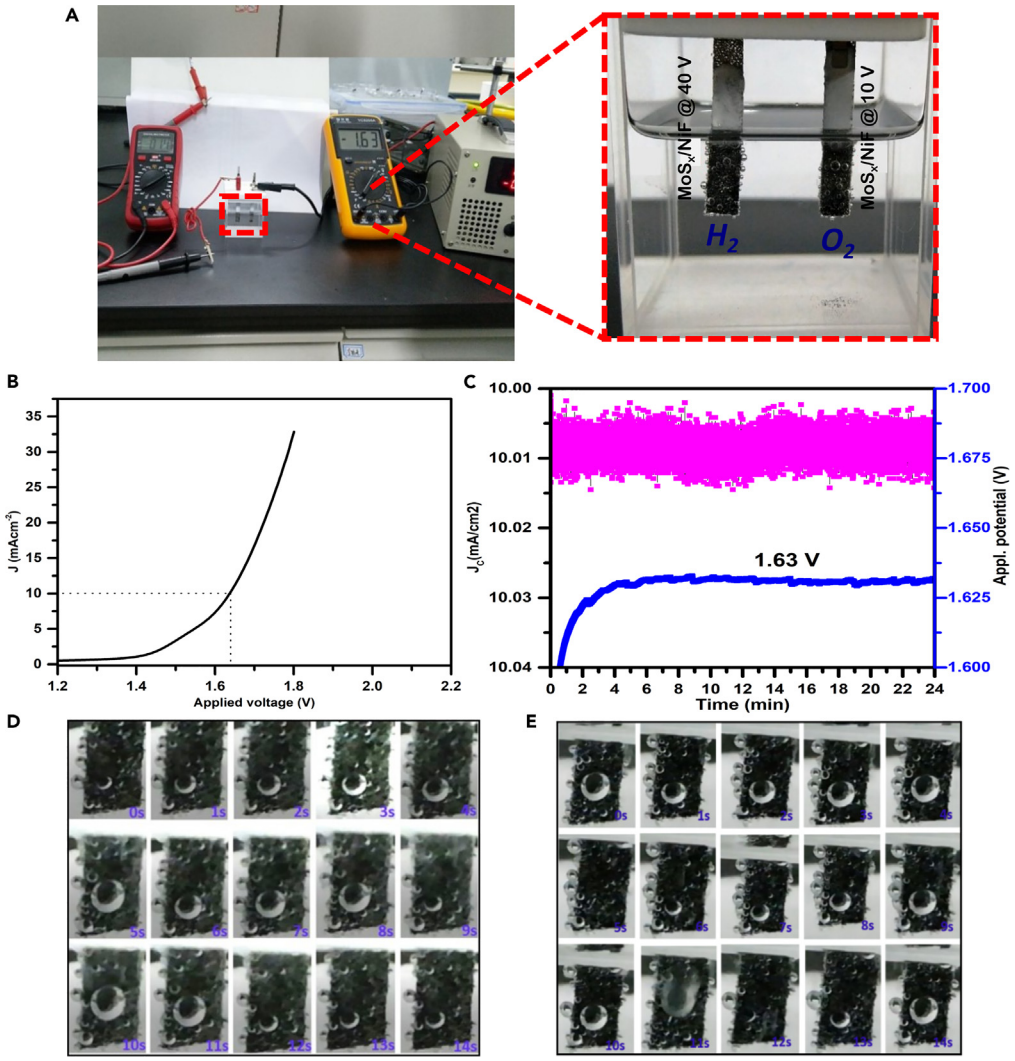

Figure 6. Overall water splitting performance for the electrochemical cell made at MoS_{2-x} NPs @ −40 V and (MoS_{2-x} NPs @ −10 V) as cathode and anode in alkaline medium

(A–E) (A) Two electrode experimental setup (full and enlarged view), (B) polarization curve, (C) long-term stability through chronoamperometry (D) hydrogen, and (E) oxygen gases at cathode (MoS_{2-x} NPs @ −40 V) and anode (MoS_{2-x} NPs @ −10 V), respectively.

The experimental OER results demonstrated that the MoS_x electrocatalyst with the lower S-vacancy site was more efficient. To understand the mechanism involved behind this, we calculated the Gibbs free energy (ΔG_{OH^*}) for OH*, one of the three OER intermediates, adsorption on the surface of stoichiometric (0% S-vacant) and 21.7% S-vacant MoS_2 (002) surface (theoretical model Figure 7C). The ΔG_{OH^*} values for the stoichiometric and 21.7% S-vacant MoS_2 are −1.48 and −3.88, respectively (Figure 7D). The increase in the ΔG_{OH^*} value with an increase in the S-vacancy in MoS_x can be one of the possible reasons for the lower experimental OER performance of the higher S-vacant MoS_x electrocatalyst.

Conclusion and outlook

In summary, we report a single-step, environment-friendly and top-down approach of electric-field assisted pulsed laser ablation of MoS_2 target in water for simultaneous control of S-vacancy, electrocatalytic active sites, in MoS_x nanoparticles and their *in-situ* dielectrophoretic deposition on nickel foam to fabricate ready to use, without any post-processing or loading on an electrode or adhesive coating, electrocatalysts on support for overall water splitting. As demonstrated experimentally, the increase in the intensity of applied external electric field decreases the size of NPs, increases formation of 3D-hierarchical architecture of MoS_x

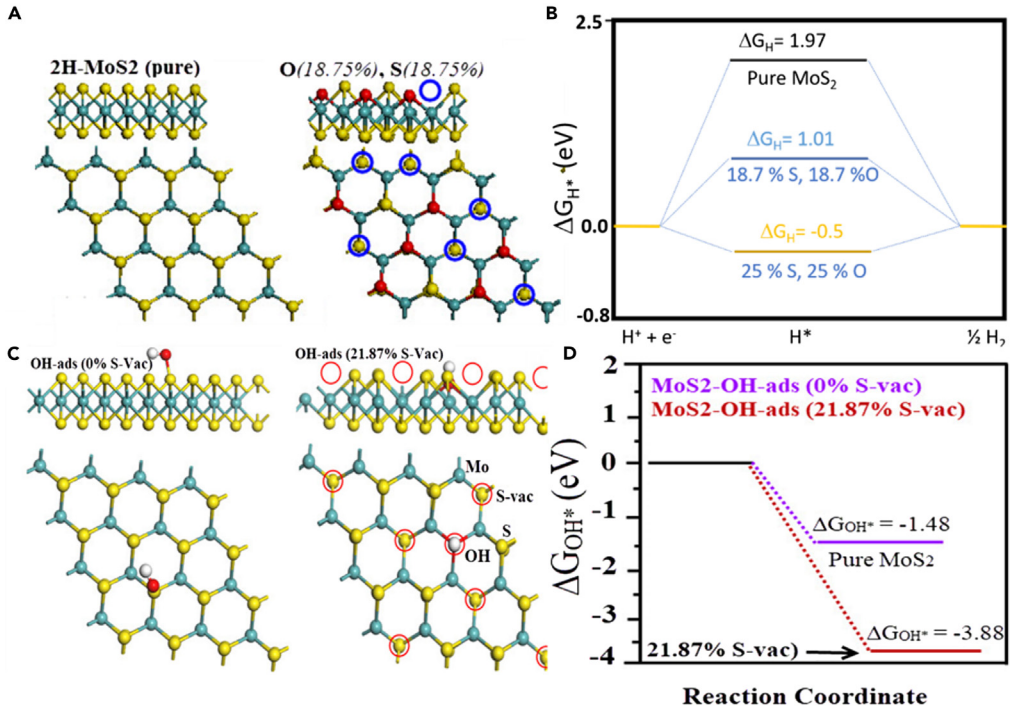

Figure 7. DFT-calculated Gibbs free energies

(A) Intrinsic and Sulfur vacant structure for the adsorption of H* radical in HER.

(B–D) (B) Gibbs free energy (ΔG_H) for H* adsorption on MoS_{2-x} NPs with x = 0, 0.1, and 0.3, (C) structure for OH*, O*, and OOH* adsorption, (D) Gibbs Free energy (ΔG_H) for different oxygen intermediate adsorption on MoS_{2-x} surface with x = 0, 0.1, and 0.3 and H_2O adsorption energy on MoS_{2-x} surface with x = 0, 0.1, and 0.3 values.

through self-assembling spherical MoS_x NPs on the Ni foam, and increases the density of S-vacancy sites in the as-produced MoS_x NPs. A higher value of applied electric field produced a higher density of S-vacancy sites in the MoS_x NPs, unveiling a larger density of Mo sites, at the surface as well as in the volume of NPs, for the adsorption of H* with a comparatively lower ΔG_{H^*} resulting in a high cathodic current density of 150 mA/cm^2 at an overpotential of ~310 mV with the Tafel slope as low as 66 mV/dec. Conversely, MoS_x/NiF electrocatalyst sample fabricated at the lowest applied electric field is found most suitable for the oxygen evolution reaction with the Tafel slope as low as 71 mV/dec. The experimental HER and OER results are supported by the theoretical calculation for the Gibbs free energies for H* (ΔG_{H^*}) and OH* (ΔG_{OH^*}) adsorptions on the surface of stochiometric and S-vacant MoS_2 electrocatalysts. Based on the experimental HER and OER results, when MoS_x/NiF/40 electrocatalyst with the highest S-vacancy sites and MoS_x/NiF/10 electrocatalyst with the lowest S-vacancy sites are coupled together as cathode and anodes, respectively in a two-electrode alkaline electrolyze cell, it requires only 1.63 V of potential to drive 10 mA/cm^2 of current density.

The density of S-vacancy in the MoS_x/NiF electrocatalysts and consequently HER efficiency can be further increased by increasing the intensity of the applied electric field. Similarly, the OER efficiency can be further increased through increasing S/Mo ratio, even beyond the stoichiometric value 2, by applying lower electric field intensity and using S containing liquid precursor. We believe the present work may be used as a guidance to rationally design and develop low-cost electrocatalysts for industrial-scale hydrogen and oxygen productions from electrocatalytic water splitting and can be extended to other electrocatalysts for wealth of chemical reactions.

Limitations of the study

Based on the combination of EDS, XPS, and DFT, sulfur vacancy has been interpreted as a key contributor to the excellent HER and OER activity and stability. However, to get an in-depth sight of the effect of sulfur vacancy, an *in-situ* characterization of the sulfur vacancy is still needed but is very challenging.

STAR★METHODS

Detailed methods are provided in the online version of this paper and include the following:

- KEY RESOURCES TABLE
- RESOURCE AVAILABILITY
  - Lead contact
  - Materials availability
  - Data and code availability
- METHOD DETAILS
  - Fabrication of MoS_x/NiF electrocatalysts
  - Characterization of electrocatalysts
  - Electrochemical measurements
  - Density functional theoretical calculation
  - Calculation of energy bandgap
  - Calculation of turnover frequency (TOF)

SUPPLEMENTAL INFORMATION

Supplemental information can be found online at https://doi.org/10.1016/j.isci.2023.106797.

ACKNOWLEDGMENTS

We would like to thank the National Natural Science Foundation of China (grant numbers 62134009 and 62121005), the Changchun Institute of Optics, Fine Mechanics, and Physics (CIOMP) Innovation Grant, the Jilin Provincial Science and Technology Development Project (grant number YDZJ202102CXJD002), and the Bill & Melinda Gates Foundation for their financial support (grant no: OPP1157723).

AUTHOR CONTRIBUTIONS

S.C.S. came with the initial idea, defined the project, and prepared the schematics. S.C.S. and C.S.S. analyzed the data, organized the figures, and wrote the manuscript. C.S.S. performed the experiments. R.A. performed theoretical calculations. C.S.S. and S.C.S. worked together in the submission and revision of the manuscript. A.S., G.V., T.T.Z., and W.Y. assisted in experiments. S.C.S., W.L., and C.G. supervised the project.

DECLARATION OF INTERESTS

The authors declare no competing interests.

INCLUSION AND DIVERSITY

We support the inclusive, diverse, and equitable conduct of research.

Received: November 13, 2022
Revised: March 31, 2023
Accepted: April 27, 2023
Published: May 4, 2023

REFERENCES

1. Singh, S.C., Li, H., Yao, C., Zhan, Z., Yu, W., Yu, Z., and Guo, C. (2018). Structural and compositional control in copper selenide nanocrystals for light-induced self-repairable electrodes. Nano Energy *51*, 774–785. https://doi.org/10.1016/j.nanoen.2018.07.020.

2. Perera, A.T.D., Nik, V.M., Chen, D., Scartezzini, J.L., and Hong, T. (2020). Quantifying the impacts of climate change and extreme climate events on energy systems. Nat. Energy *5*, 150–159. https://doi.org/10.1038/s41560-020-0558-0.

3. Arbabzadeh, M., Sioshansi, R., Johnson, J.X., and Keoleian, G.A. (2019). The role of energy storage in deep decarbonization of electricity production. Nat. Commun. *10*, 3413–3511. https://doi.org/10.1038/s41467-019-11161-5.

4. Saraj, C.S., Singh, S.C., Verma, G., Rajan, R.A., Li, W., and Guo, C. (2022). Laser-induced periodic surface structured electrodes with 45% energy saving in electrochemical fuel generation through field localization. Opto-Electronic Adv. *5*, 210105. https://doi.org/10.29026/oea.2022.210105.

5. Hisatomi, T., and Domen, K. (2019). Reaction systems for solar hydrogen production via water splitting with particulate semiconductor photocatalysts. Nat. Catal. *2*, 387–399. https://doi.org/10.1038/s41929-019-0242-6.

6. Li, S., Xi, C., Jin, Y.Z., Wu, D., Wang, J.Q., Liu, T., Wang, H.B., Dong, C.K., Liu, H., Kulinich, S.A., and Du, X.W. (2019). Ir-O-V catalytic group in Ir-doped NiV(OH)2 for overall water splitting. ACS Energy Lett. *4*, 1823–1829. https://doi.org/10.1021/acsenergylett.9b01252.

7. Luo, X., Ji, P., Wang, P., Cheng, R., Chen, D., Lin, C., Zhang, J., He, J., Shi, Z., Li, N., et al. (2020). Interface engineering of hierarchical branched Mo-doped Ni3S2/NixPy hollow heterostructure nanorods for efficient overall

water splitting. Adv. Energy Mater. *10*, 1903891–1903911. https://doi.org/10.1002/aenm.201903891.

8. Saraj, C.S., Singh, S.C., Shukla, A., Yu, W., Fayyaz, M.U., and Guo, C. (2021). Single-step and sustainable fabrication of Ni(OH) 2/Ni foam water splitting catalysts via electric field assisted pulsed laser ablation in liquid. Chemelectrochem *8*, 209–217. https://doi.org/10.1002/celc.202001511.

9. Subbaraman, R., Tripkovic, D., Strmcnik, D., Chang, K.C., Uchimura, M., Paulikas, A.P., Stamenkovic, V., and Markovic, N.M. (2011). Enhancing hydrogen evolution activity in water splitting by tailoring Li+-Ni(OH)2-Pt interfaces. Science *334*, 1256–1260. https://doi.org/10.1126/science.1211934.

10. Shan, J., Ling, T., Davey, K., Zheng, Y., and Qiao, S.Z. (2019). Transition-metal-Doped RuIr bifunctional nanocrystals for overall water splitting in acidic environments. Adv. Mater. *31*, e1900510–e1900517. https://doi.org/10.1002/adma.201900510.

11. Willinger, E., Massué, C., Schlögl, R., and Willinger, M.G. (2017). Identifying key structural features of IrOx water splitting catalysts. J. Am. Chem. Soc. *139*, 12093–12101. https://doi.org/10.1021/jacs.7b07079.

12. Shukla, A., Singh, S.C., Saraj, C.S., Verma, G., and Guo, C. (2022). Ni-based overall water splitting electrocatalysts prepared via laser-ablation-in-liquids combined with electrophoretic deposition. Mater. Today Chem. *23*, 100691. https://doi.org/10.1016/j.mtchem.2021.100691.

13. Arif, A., Xu, M., Rashid, J., Saraj, C.S., Li, W., Akram, B., and Hu, B. (2021). Efficient recovery of lithium cobaltate from spent lithium-ion batteries for oxygen evolution reaction. Nanomaterials *11*, 3343. https://doi.org/10.3390/nano11123343.

14. Yu, Y., Lee, S.J., Theerthagiri, J., Lee, Y., and Choi, M.Y. (2022). Architecting the AuPt alloys for hydrazine oxidation as an anolyte in fuel cell: comparative analysis of hydrazine splitting and water splitting for energy-saving H2 generation. Appl. Catal. B Environ. *316*, 121603. https://doi.org/10.1016/j.apcatb.2022.121603.

15. Sarkar, S., and Peter, S.C. (2018). An overview on Pd-based electrocatalysts for the hydrogen evolution reaction. Inorg. Chem. Front. *5*, 2060–2080. https://doi.org/10.1039/c8qi00042e.

16. Jiang, Z., Ren, J., Li, Y., Zhang, X., Zhang, P., Huang, J., Du, C., and Chen, J. (2019). Low-cost high-performance hydrogen evolution electrocatalysts based on Pt-CoP polyhedra with low Pt loading in both alkaline and neutral media. Dalton Trans. *48*, 8920–8930. https://doi.org/10.1039/c9dt01118h.

17. Bae, S.Y., Mahmood, J., Jeon, I.Y., and Baek, J.B. (2020). Recent advances in ruthenium-based electrocatalysts for the hydrogen evolution reaction. Nanoscale Horiz. *5*, 43–56. https://doi.org/10.1039/c9nh00485h.

18. Kanwal, N., Akram, B., Saraj, C.S., Ahmad, K., Talib, S.H., and Asif, H.M. (2022). Counterion-controlled synthesis of multifunctional iron cobalt mixed oxide laminar superstructures. New J. Chem. *46*, 9762–9766. https://doi.org/10.1039/D2NJ00412G.

19. Song, H.J., Yoon, H., Ju, B., Lee, G.H., and Kim, D.W. (2018). 3D architectures of quaternary Co-Ni-S-P/graphene hybrids as highly active and stable bifunctional electrocatalysts for overall water splitting. Adv. Energy Mater. *8*, 1802319–1802410. https://doi.org/10.1002/aenm.201802319.

20. Anjum, M.A.R., Okyay, M.S., Kim, M., Lee, M.H., Park, N., and Lee, J.S. (2018). Bifunctional sulfur-doped cobalt phosphide electrocatalyst outperforms all-noble-metal electrocatalysts in alkaline electrolyzer for overall water splitting. Nano Energy *53*, 286–295. https://doi.org/10.1016/j.nanoen.2018.08.064.

21. Yu, W., Yin, J., Li, Y., Lai, B., Jiang, T., Li, Y., Liu, H., Liu, J., Zhao, C., Singh, S.C., et al. (2019). Ag2S quantum dots as an infrared excited photocatalyst for hydrogen production. ACS Appl. Energy Mater. *2*, 2751–2759. https://doi.org/10.1021/acsaem.9b00091.

22. Dastafkan, K., Li, Y., Zeng, Y., Han, L., and Zhao, C. (2019). Enhanced surface wettability and innate activity of an iron borate catalyst for efficient oxygen evolution and gas bubble detachment. J. Mater. Chem. *7*, 15252–15261. https://doi.org/10.1039/c9ta03346g.

23. Yang, W., Dastafkan, K., Jia, C., and Zhao, C. (2018). Design of electrocatalysts and electrochemical cells for carbon dioxide reduction reactions. Adv. Mater. Technol. *3*, 1700377–1700420. https://doi.org/10.1002/admt.201700377.

24. Zhang, Y., Yin, P.F., Liu, X.H., Mao, J., Kulinich, S.A., and Du, X.W. (2017). Tuning band structure of cadmium chalcogenide nanoflake arrays via alloying for efficient photoelectrochemical hydrogen evolution. Langmuir *33*, 6457–6463. https://doi.org/10.1021/acs.langmuir.7b00878.

25. Zhang, Y., Shao, Q., Long, S., and Huang, X. (2018). Cobalt-molybdenum nanosheet arrays as highly efficient and stable earth-abundant electrocatalysts for overall water splitting. Nano Energy *45*, 448–455. https://doi.org/10.1016/j.nanoen.2018.01.022.

26. Li, H., Wen, P., Li, Q., Dun, C., Xing, J., Lu, C., Adhikari, S., Jiang, L., Carroll, D.L., and Geyer, S.M. (2017). Earth-abundant iron diboride (FeB2) nanoparticles as highly active bifunctional electrocatalysts for overall water splitting. Adv. Energy Mater. *7*, 1700513–1700612. https://doi.org/10.1002/aenm.201700513.

27. Theerthagiri, J., Karuppasamy, K., Lee, S.J., Shwetharani, R., Kim, H.S., Pasha, S.K.K., Ashokkumar, M., and Choi, M.Y. (2022). Fundamentals and comprehensive insights on pulsed laser synthesis of advanced materials for diverse photo- and electrocatalytic applications. Light Sci. Appl. *11*, 250. https://doi.org/10.1038/s41377-022-00904-7.

28. Lai, B., Singh, S.C., Bindra, J.K., Saraj, C.S., Shukla, A., Yadav, T.P., Wu, W., McGill, S.A., Dalal, N.S., Srivastava, A., and Guo, C. (2019). Hydrogen evolution reaction from bare and surface-functionalized few-layered MoS2 nanosheets in acidic and alkaline electrolytes. Mater. Today Chem. *14*, 100207. https://doi.org/10.1016/j.mtchem.2019.100207.

29. Hai, X., Zhou, W., Wang, S., Pang, H., Chang, K., Ichihara, F., and Ye, J. (2017). Rational design of freestanding MoS2 monolayers for hydrogen evolution reaction. Nano Energy *39*, 409–417. https://doi.org/10.1016/j.nanoen.2017.07.021.

30. Tang, S., Wu, W., Zhang, S., Ye, D., Zhong, P., Li, X., Liu, L., and Li, Y.F. (2018). Tuning the activity of the inert MoS2 surface via graphene oxide support doping towards chemical functionalization and hydrogen evolution: a density functional study. Phys. Chem. Chem. Phys. *20*, 1861–1871. https://doi.org/10.1039/c7cp06636h.

31. Yang, Y., Zhang, K., Lin, H., Li, X., Chan, H.C., Yang, L., and Gao, Q. (2017). MoS2-Ni3S2 heteronanorods as efficient and stable bifunctional electrocatalysts for overall water splitting. ACS Catal. *7*, 2357–2366. https://doi.org/10.1021/acscatal.6b03192.

32. Muthurasu, A., Maruthapandian, V., and Kim, H.Y. (2019). Metal-organic framework derived Co3O4/MoS2 heterostructure for efficient bifunctional electrocatalysts for oxygen evolution reaction and hydrogen evolution reaction. Appl. Catal. B Environ. *248*, 202–210. https://doi.org/10.1016/j.apcatb.2019.02.014.

33. Merki, D., and Hu, X. (2011). Recent developments of molybdenum and tungsten sulfides as hydrogen evolution catalysts. Energy Environ. Sci. *4*, 3878–3888. https://doi.org/10.1039/c1ee01970h.

34. Saraj, C.S., Singh, S.C., Verma, G., Alquliah, A., Li, W., and Guo, C. (2023). Rapid fabrication of CuMoO4 nanocomposites via electric field assisted pulsed-laser ablation in liquids for electrochemical hydrogen generation. Appl. Surf. Sci. Adv. *13*, 100358. https://doi.org/10.1016/j.apsadv.2022.100358.

35. Jaramillo, T.F., Jørgensen, K.P., Bonde, J., Nielsen, J.H., Horch, S., and Chorkendorff, I. (2007). Identification of active edge sites for electrochemical H2 evolution from MoS2 nanocatalysts. Science *317*, 100–102. https://doi.org/10.1126/science.1141483.

36. Xue, X., Zhang, J., Saana, I.A., Sun, J., Xu, Q., and Mu, S. (2018). Rational inert-basal-plane activating design of ultrathin 1T′ phase MoS2 with a MoO3 heterostructure for enhancing hydrogen evolution performances. Nanoscale *10*, 16531–16538. https://doi.org/10.1039/c8nr05270k.

37. Gong, M., Li, Y., Wang, H., Liang, Y., Wu, J.Z., Zhou, J., Wang, J., Regier, T., Wei, F., and Dai, H. (2013). An advanced Ni-Fe layered double hydroxide electrocatalyst for water oxidation. J. Am. Chem. Soc. *135*, 8452–8455. https://doi.org/10.1021/ja4027715.

38. Kong, D., Wang, H., Cha, J.J., Pasta, M., Koski, K.J., Yao, J., and Cui, Y. (2013). Synthesis of MoS 2 and MoSe 2 Films with

Vertically Aligned Layers. Nano Lett. *13*, 1341–1347. https://doi.org/10.1021/nl400258t.

39. Benson, J., Li, M., Wang, S., Wang, P., and Papakonstantinou, P. (2015). Electrocatalytic hydrogen evolution reaction on edges of a few layer molybdenum disulfide nanodots. ACS Appl. Mater. Interfaces *7*, 14113–14122. https://doi.org/10.1021/acsami.5b03399.

40. Tsai, C., Abild-Pedersen, F., and Nørskov, J.K. (2014). Tuning the MoS2 edge-site activity for hydrogen evolution via support interactions. Nano Lett. *14*, 1381–1387. https://doi.org/10.1021/nl404444k.

41. Chen, Z., Cummins, D., Reinecke, B.N., Clark, E., Sunkara, M.K., and Jaramillo, T.F. (2011). Core-shell MoO3-MoS2 nanowires for hydrogen evolution: a functional design for electrocatalytic materials. Nano Lett. *11*, 4168–4175. https://doi.org/10.1021/nl2020476.

42. Xie, J., Zhang, H., Li, S., Wang, R., Sun, X., Zhou, M., Zhou, J., Lou, X.W.D., and Xie, Y. (2013). Defect-rich MoS2 ultrathin nanosheets with additional active edge sites for enhanced electrocatalytic hydrogen evolution. Adv. Mater. *25*, 5807–5813. https://doi.org/10.1002/adma.201302685.

43. Kibsgaard, J., Chen, Z., Reinecke, B.N., and Jaramillo, T.F. (2012). Engineering the surface structure of MoS 2 toÂ preferentially expose active edge sites forÂ electrocatalysis. Nat. Mater. *11*, 963–969. https://doi.org/10.1038/nmat3439.

44. Shahid, M.Z., Mehmood, R., Athar, M., Hussain, J., Wei, Y., and Khaliq, A. (2021). BiOCl nanoplates doped with Fe3+Ions for the visible-light degradation of aqueous pollutants. ACS Appl. Nano Mater. *4*, 746–758. https://doi.org/10.1021/acsanm.0c03042.

45. Russell, A.E. (2008). Faraday discussions: preface. Faraday Discuss *140*, 9–10. https://doi.org/10.1039/b814058h.

46. Wang, H.Y., Lin, C.K., Kong, D., Chan, K., Abild-Pedersen, F., Nørskov, J.K., and Cui, Y. (2015). Transition-metal doped edge sites in vertically aligned MoS2 catalysts for enhanced hydrogen evolution. Nano Res. *117*, 566–579. https://doi.org/10.1007/s12274-014-0677-7.

47. Zhang, H., Li, Y., Yao, X., Liang, G., and Yu, D. (2017). Small dopants make big differences: enhanced electrocatalytic performance of MoS2 monolayer for oxygen reduction reaction (ORR) by N– and P–doping. Plant Physiol. *175*, 543–554. https://doi.org/10.1016/j.electacta.2016.12.144.

48. Bai, X., Li, Q., Shi, L., Ling, C., and Wang, J. (2020). Edge promotion and basal plane activation of MoS2 catalyst by isolated Co atoms for hydrodesulfurization and hydrodenitrogenation. Catal. Today *350*, 56–63. https://doi.org/10.1016/j.cattod.2019.07.049.

49. Ouyang, Y., Ling, C., Chen, Q., Wang, Z., Shi, L., and Wang, J. (2016). Activating inert basal planes of MoS2 for hydrogen evolution reaction through the formation of different intrinsic defects. Chem. Mater. *28*, 4390–4396. https://doi.org/10.1021/acs.chemmater.6b01395.

50. Hu, C., Jiang, Z., Zhou, W., Guo, M., Yu, T., Luo, X., and Yuan, C. (2019). Wafer-scale sulfur vacancy-rich monolayer MoS2 for massive hydrogen production. J. Phys. Chem. Lett. *10*, 4763–4768. https://doi.org/10.1021/acs.jpclett.9b01399.

51. Tsai, C., Li, H., Park, S., Park, J., Han, H.S., Nørskov, J.K., Zheng, X., and Abild-Pedersen, F. (2017). Electrochemical generation of sulfur vacancies in the basal plane of MoS2 for hydrogen evolution. Nat. Commun. *8*, 15113–15118. https://doi.org/10.1038/ncomms15113.

52. Li, H., Tsai, C., Koh, A.L., Cai, L., Contryman, A.W., Fragapane, A.H., Zhao, J., Han, H.S., Manoharan, H.C., Abild-Pedersen, F., et al. (2016). Correction: Activating and optimizing MoS2 basal planes for hydrogen evolution through the formation of strained sulphur vacancies. Nat. Mater. *15*, 364. https://doi.org/10.1038/nmat4564.

53. Cheng, C.C., Lu, A.Y., Tseng, C.C., Yang, X., Hedhili, M.N., Chen, M.C., Wei, K.H., and Li, L.J. (2016). Activating basal-plane catalytic activity of two-dimensional MoS2 monolayer with remote hydrogen plasma. Nano Energy *30*, 846–852. https://doi.org/10.1016/j.nanoen.2016.09.010.

54. Li, H., Tsai, C., Koh, A.L., Cai, L., Contryman, A.W., Fragapane, A.H., Zhao, J., Han, H.S., Manoharan, H.C., Abild-Pedersen, F., et al. (2016). Activating and optimizing MoS2 basal planes for hydrogen evolution through the formation of strained sulphur vacancies. Nat. Mater. *15*, 48–53. https://doi.org/10.1038/nmat4465.

55. Verma, G., Yadav, G., Saraj, C.S., Li, L., Miljkovic, N., Delville, J.P., and Li, W. (2022). A versatile interferometric technique for probing the thermophysical properties of complex fluids. Light Sci. Appl. *11*, 115. https://doi.org/10.1038/s41377-022-00796-7.

56. Liu, P., Wang, C.X., Chen, X.Y., and Yang, G.W. (2008). Controllable fabrication and cathodoluminescence performance of high-index facets GeO2 micro- and nanocubes and spindles upon electrical-field-assisted laser ablation in liquid. J. Phys. Chem. C *112*, 13450–13456. https://doi.org/10.1021/jp802529r.

57. Singh, S.C., and Gopal, R. (2008). Laser irradiance and wavelength-dependent compositional evolution of inorganic ZnO and ZnOOH/organic SDS nanocomposite material. J. Phys. Chem. C *112*, 2812–2819. https://doi.org/10.1021/jp0753676.

58. Singh, N.B., Amist, N., Yadav, K., Singh, D., Pandey, J.K., and Singh, S.C. (2013). Zinc oxide nanoparticles as fertilizer for the germination, growth and metabolism of vegetable crops. J. Nanoengng. Nanomfg. *3*, 353–364. https://doi.org/10.1166/jnan.2013.1156.

59. Singh, S.C., and Gopal, R. (2008). Synthesis of colloidal zinc oxide nanoparticles by pulsed laser ablation in aqueous media. Phys. E Low-dimensional Syst. Nanostructures *40*, 724–730. https://doi.org/10.1016/j.physe.2007.08.155.

60. Singh, D., Kumar, S., Singh, S.C., Lal, B., and Singh, N.B. (2012). Applications of liquid assisted pulsed laser ablation synthesized TiO2 nanoparticles on germination, growth and biochemical parameters of Brassica oleracea var. Sci. Adv. Mater. *4*, 522–531.

61. Singh, S.C., Swarnkar, R.K., and Gopal, R. (2010). Zn/ZnO core/shell nanoparticles synthesized by laser ablation in aqueous environment: optical and structural characterizations. Bull. Mater. Sci. *33*, 21–26. https://doi.org/10.1007/s12034-010-0003-2.

62. Naik Shreyanka, S., Theerthagiri, J., Lee, S.J., Yu, Y., and Choi, M.Y. (2022). Multiscale design of 3D metal–organic frameworks (M−BTC, M: Cu, Co, Ni) via PLAL enabling bifunctional electrocatalysts for robust overall water splitting. Chem. Eng. J. *446*, 137045. https://doi.org/10.1016/j.cej.2022.137045.

63. Singh, S.C., Kotnala, R.K., and Gopal, R. (2015). Room temperature ferromagnetism in liquid-phase pulsed laser ablation synthesized nanoparticles of nonmagnetic oxides. J. Appl. Phys. *118*, 064305–064307. https://doi.org/10.1063/1.4928312.

64. Zeng, H., Du, X.W., Singh, S.C., Kulinich, S.A., Yang, S., He, J., and Cai, W. (2012). Nanomaterials via laser ablation/irradiation in liquid: a review. Adv. Funct. Mater. *22*, 1333–1353. https://doi.org/10.1002/adfm.201102295.

65. Swarnkar, R.K., Singh, S.C., Gopal, R., Singh, M.R., and Lipson, R.H. (2009). Synthesis of copper/copper-oxide nanoparticles: optical and structural characterizations. AIP Conf. Proc. *1147*, 205–210. https://doi.org/10.1063/1.3183432.

66. Singh, S.C. (2011). Effect of oxygen injection on the size and compositional evolution of ZnO/Zn(OH)2 nanocomposite synthesized by pulsed laser ablation in distilled water. J. Nano Res. *13*, 4143–4152. https://doi.org/10.1007/s11051-011-0359-2.

67. Singh, S.C., Swarnkar, R.K., and Gopal, R. (2009). Synthesis of titanium dioxide nanomaterial by pulsed laser ablation in water. J. Nanosci. Nanotechnol. *9*, 5367–5371.

68. Singh, S.C., Swarnkar, R.K., and Gopal, R. (2009). Laser ablative approach for the synthesis of cadmium hydroxide–oxide nanocomposite. J. Nano Res. *11*, 1831–1838. https://doi.org/10.1007/s11051-009-9696-9.

69. Singh, S.C., Fallon, C., Hayden, P., Mujawar, M., Yeates, P., and Costello, J.T. (2014). Ion flux enhancements and oscillations in spatially confined laser produced aluminum plasmas. Phys. Plasmas *21*, 093113. https://doi.org/10.1063/1.4895601.

70. Menéndez-Manjón, A. (2009). Mobility of nanoparticles generated by femtosecond laser ablation in liquids and its application to surface patterning. J. Laser

Micro/Nanoengineering *4*, 95–99. https://doi.org/10.2961/jlmn.2009.02.0004.

71. Chen, X., Zhu, X., Xiao, W., Liu, G., Feng, Y.P., Ding, J., and Li, R.W. (2015). Nanoscale magnetization reversal caused by electric field-induced ion migration and redistribution in cobalt ferrite thin films. ACS Nano *9*, 4210–4218. https://doi.org/10.1021/acsnano.5b00456.

72. Compagnini, G., Sinatra, M., Russo, P., Messina, G.C., Puglisi, O., and Scalese, S. (2012). Deposition of few layer graphene nanowalls at the electrodes during electric field-assisted laser ablation of carbon in water. Carbon N. Y. *50*, 2362–2365. https://doi.org/10.1016/j.carbon.2012.01.038.

73. Liu, P., Liang, Y., Lin, X., Wang, C., and Yang, G. (2011). A general strategy to fabricate simple polyoxometalate nanostructures: electrochemistry-assisted laser ablation in liquid. ACS Nano *5*, 4748–4755. https://doi.org/10.1021/nn2007282.

74. Chikan, V., and Kelley, D.F. (2002). Size-dependent spectroscopy of MoS2 nanoclusters. J. Phys. Chem. B *106*, 3794–3804. https://doi.org/10.1021/jp011898x.

75. Wilcoxon, J.P., Newcomer, P.P., and Samara, G.A. (1997). Synthesis and optical properties of MoS2 and isomorphous nanoclusters in the quantum confinement regime. J. Appl. Phys. *81*, 7934–7944. https://doi.org/10.1063/1.365367.

76. Wilcoxon, J.P., and Samara, G.A. (1995). Strong quantum-size effects in a layered semiconductor: MoS2 nanoclusters. Phys. Rev. B *51*, 7299–7302. https://doi.org/10.1103/PhysRevB.51.7299.

77. Li, B., Jiang, L., Li, X., Ran, P., Zuo, P., Wang, A., Qu, L., Zhao, Y., Cheng, Z., and Lu, Y. (2017). Preparation of monolayer MoS2 quantum dots using temporally shaped femtosecond laser ablation of bulk MoS2 targets in water. Sci. Rep. *7*, 11182–11212. https://doi.org/10.1038/s41598-017-10632-3.

78. Singh, S.C., Mishra, S.K., Srivastava, R.K., and Gopal, R. (2010). Optical properties of selenium quantum dots produced with laser irradiation of water suspended Se nanoparticles. J. Phys. Chem. C *114*, 17374–17384. https://doi.org/10.1021/jp105037w.

79. Singh, S.C., and Gopal, R. (2012). Drop shaped zinc oxide quantum dots and their self-assembly into dendritic nanostructures: liquid assisted pulsed laser ablation and characterizations. Appl. Surf. Sci. *258*, 2211–2218. https://doi.org/10.1016/j.apsusc.2011.05.018.

80. Singh, S.C., and Gopal, R. (2010). Nanoarchitectural evolution from laser-produced colloidal solution: growth of various complex cadmium hydroxide architectures from simple particles. J. Phys. Chem. C *114*, 9277–9289. https://doi.org/10.1021/jp1018907.

81. Zhang, J., Wang, T., Pohl, D., Rellinghaus, B., Dong, R., Liu, S., Zhuang, X., and Feng, X. (2016). Interface engineering of MoS2/Ni3S2Heterostructures for highly enhanced electrochemical overall-water-splitting activity. Angew. Chem., Int. Ed. Engl. *55*, 6702–6707. https://doi.org/10.1002/anie.201602237.

82. Benck, J.D., Hellstern, T.R., Kibsgaard, J., Chakthranont, P., and Jaramillo, T.F. (2014). Catalyzing the hydrogen evolution reaction (HER) with molybdenum sulfide nanomaterials. ACS Catal. *4*, 3957–3971. https://doi.org/10.1021/cs500923c.

83. Voiry, D., Salehi, M., Silva, R., Fujita, T., Chen, M., Asefa, T., Shenoy, V.B., Eda, G., and Chhowalla, M. (2013). Conducting MoS2 nanosheets as catalysts for hydrogen evolution reaction. Nano Lett. *13*, 6222–6227. https://doi.org/10.1021/nl403661s.

84. Li, J.-S., Wang, Y., Liu, C.-H., Li, S.-L., Wang, Y.-G., Dong, L.-Z., Dai, Z.-H., Li, Y.-F., and Lan, Y.-Q. (2016). Coupled molybdenum carbide and reduced graphene oxide electrocatalysts for efficient hydrogen evolution. Nat. Commun. *7*, 11204. https://doi.org/10.1038/ncomms11204.

STAR★METHODS

KEY RESOURCES TABLE

REAGENT or RESOURCE	SOURCE	IDENTIFIER
Chemicals, peptides, and recombinant proteins		
KOH	Macklin	CAS#1310-58-3
Nickel foam	Sigma Aldrich	CAS#7440-02-0
MoS_2 target	Sigma Aldrich	CAS#1317-33-5
Pt/C 20%	Macklin	CAS#7440-06-4
Ruthenium (iv) oxide	Macklin	CAS#12036-10-1
Software and algorithms		
Inkscape	Open source	https://inkscape.org
ImageJ	Open source	https://imagej.org
other		
Biologic electrochemical workstation	France	https://www.biologic.net

RESOURCE AVAILABILITY

Lead contact

Information and requests for resources should be directed to and will be fulfilled by lead author, Wei Li (weili1@ciomp.ac.cn (W.L)).

Materials availability

This study did not generate new unique reagents. All chemicals were obtained from commercial resources and used as received.

Data and code availability

- All data reported in this paper will be shared by the lead contact upon request.
- This study does not generate a new code.
- Any additional information required to reanalyze the data reported in this study is available from the lead contact upon request.

METHOD DETAILS

Fabrication of MoS_x/NiF electrocatalysts

MoS_x/NiF electrocatalysts were fabricated by irradiating a pulsed laser beam on the surface of a MoS_2 target, submerged in water, while simultaneously applying an external electric field. A solid disc of MoS_2 (diameter; 3 cm) was placed at the bottom of a glass container with a 2 cm thick water layer on the target surface. The disc was irradiated with a laser beam from a Spectra-Physics Spitfire fs-laser system delivering pulses at 800 nm wavelength, 200 ps pulse duration, 1 kHz repetition rate, and 0.5 $mJ/pulse\ energy$. A 50 cm focal length plano-convex lens was employed to focus the laser beam at the target surface. To ensure that each laser pulse ablates a new surface, the glass container was mounted on a motorized X-Y translational stage and moved at a speed of 1 mm/s. The electric field across the laser produced plasma responsible for S vacancy generation and dielectrophoretic deposition was produced by biasing of a pair of parallel Ni-foam electrodes (size: 30 mm*5 mm*1 mm) with 1 cm separation. The electric field value varied from 10 V/cm – 40 V/cm by varying the dc biasing voltage between the electrodes while maintaining the distance between them. Each sample was produced using ablation and dielectrophoretic deposition for sixty minutes.

Characterization of electrocatalysts

The UV-visible absorption spectra of the colloidal solution of NPs were measured in the spectral region of 200–800 nm using a Cary 300 (Agilent Technologies) double-beam spectrophotometer. The liquid samples were used for UV-visible measurements that were collected from the ablation vessel during

dielectrophoretic deposition. X-ray diffraction (XRD) measurements of the MoS_x samples were done using a Bruker-D8-Focus X-ray diffractometer with $Cu - K\alpha$ (λ = 1.5406 Å) line. The Raman spectra of different MoS_x samples were measured using a Labram HR Evolution Raman spectrometer (Horiba Jobin Yvon). The X-ray photoelectron spectra of MoS_x samples were recorded using Thermo Escalab 250XI X-ray photoelectron spectroscopy with AlKα X-ray source. For XRD, Raman and XPS measurements the electrophoretic deposition was done on ITO coated glass substrate during laser ablation. The HITACHI S4800 scanning electron microscope was used to take the SEM measurements of the MoS_x/NiF electrocatalysts under the acceleration voltage of 15 kV. All the energy-dispersive X-ray spectroscopy (EDS) spectra were also collected by mapping the electron beam at the same acceleration voltage.

Electrochemical measurements

The electrochemical measurements were carried out on a BioLogic VMP3 multichannel workstation with a three-electrode system where an EF-PLA-fabricated MoS_x/NiF electrocatalyst (1 $cm \times 0.5\ cm$) was used as a working electrode while a Ni foam and a saturated calomel electrode (SCE) were used as counter and reference electrodes, respectively. The electrolyte for all electrochemical tests was an aqueous solution of 1M KOH. Before conducting linear sweep voltammetry (LSV) curves, 30 cycles of cyclic voltammetry (CV) at a scan rate of 40 mVs^{-1} were performed for each working electrode. LSV curves were measured by sweeping voltage from 0.2 to −0.8 V vs. SCE electrode at 10 mVs^{-1}. Following equation were used to translate the potential versus SCE to versus reversible hydrogen electrode (RHE).[14,84]

$$E_{RHE} = E_{SCE} + E^0_{SCE} + 0.0592 * pH,$$

where $E^0_{SCE} = 0.243\ V$, is the Calibrated potential. The LSV curve can been seen in Figure S18. The potentials at which the current value was zero was taken as the thermodynamic potential. Therefore, for our calculation we used $E^0_{SCE} = 0.243\ V$. Electrochemical impedance spectroscopy (EIS) was performed at a dc overpotential of −0.54 V against RHE (For HER) and 1.54V vs RHE (for OER) while superimposing a tiny alternating voltage of 10 mV over the frequency range of 10 mHz to 1 MHz. The CV curves were measured in the non-Faradaic region of potential from 0.84 V to 1.04 V (versus RHE) for HER and from 1.23 V to 1.54 V (versus RHE) for OER at various scan rates (from 10 mVs^{-1} to 120 mVs^{-1} for HER and from 10 mVs^{-1} to 80 mVs^{-1} for OER) to estimate the double layer capacitance (C_{dl}) and electrochemically active surface area (ECSA). C_{dl} is the slope of the difference between the cathodic and anodic current densities $\Delta J = J_c - J_a$) as a function of the scan rate. $ESCA_{MoSx/NiF} = C_{dl\_MoSx/NiF}/C_{dl\_NiF}$; where $C_{dl\ NiF}$ is the double-layer capacitance for the bare Ni foam. Here, we used the C_{dl} value of the bare Ni foam rather than the general specific capacitance (C_s) to eliminate the effect of the greater capacitance value of bare NF. The turnover frequency (TOF) values of Mo and $S_{vacancy}$ active sites for the HER and Mo and S active sites for the OER were determined from the corresponding LSV curves and the density of the active sites was approximated using the respective ECSA values. The durability and stability of each of the electrocatalysts are tested using 24-hour chronopotentiometry (CP) test and LSV curves before and after the CP measurements.

Density functional theoretical calculation

We used density functional theory (DFT) with the Vienna ab-initio simulation software (VASP) for all the calculations. The van der Walls (vdW) interaction was employed in conjunction with the generalized gradient approximation (GGA) of the Perdew-Burke-Ernzerhof (PBE) exchange-correlation functional. The 520-eV cutoff energy of the plane wave was utilized. For simplicity, we assumed a 2H-MoS_2 monolayer (S = 32, Mo = 16 atoms) with a 4 × 4 × 1 supercell in the computations. K-points with dimensions of 2 × 2×1 was used for both structural optimization and band structure calculations. A periodic boundary conditions was used throughout the calculations and a 15 Å of vacuum is considered in the z-direction to keep the slabs apart. We followed the method described in the prior study to determine the ΔG_{H^*} for H* adsorption.[52] A 0.01 eV $Å^{-1}$ force criterion was used for the structural relaxation. We used PBE-vdW potential for the band structure calculations for consistency with the other calculations. Band structure computations were performed using the k-points of high symmetry Γ(0.0, 0.0, 0.0), M (1/2, 0.0, 0.0), and K (1/3, 1/3, 0.0).

Calculation of energy bandgap

From the UV-visible optical absorption data (Figure S1A), the absorption coefficient, α, of the colloidal solution of NPs under the Lambert-Beer's law, is related to its bandgap energy following the expression, $\alpha h\upsilon = A(h\upsilon - E_g)^n$, where A is a constant, E_g is the bandgap of the material, and the exponent n may have values 1/2, 2, 3/2, and 3 for allowed direct bandgap, allowed indirect bandgap, forbidden direct

bandgap, and forbidden indirect bandgap semiconductors respectively. [1,2] The region of fundamental absorption that corresponds to electronic transition from the top of the valance band to the bottom of the conduction band can be used to calculate the bandgap of the material and consequently the size of MoS_x NPs. Owing to its allowed direct bandgap nature (n= ½) of MoS_2 the linear region of $(\alpha h\upsilon)^2 = A(h\upsilon - E_g)$ curve, known as Tauc's plot, can be directly used to determine the bandgap of material (Figure S1C), however, several times it leads uncertainty in determining the linear portion. The $h\upsilon$ derivative of $\ln(\alpha h\upsilon) = n \ln A(h\upsilon - E_g)$ results following expression:

$$\frac{d\{\ln(\alpha h\upsilon)\}}{d(h\upsilon)} = \frac{n}{(h\upsilon - E_g)}$$

The plot of $d\{\ln(\alpha h\upsilon)\}/d(h\upsilon)$ *versus* $h\upsilon$ shows a divergence at energy equal to the bandgap energy, as shown in Figure S1D. This plot suffers comparatively less error as compared to the Tauc's plot shown in Figure S1C. The center of the corresponding peak, shown in Figure S1D, gives the band gap energy of the particles and can be used in the determination of size of particles using effective mass model as follows:

$$\Delta E_g = \left[\frac{\hbar^2}{2\mu R^2}\right] - \frac{1.8e^2}{4\pi K\varepsilon_0 R}$$

Where ΔE_g is change in the bandgap energy of the particle due to reduction in the size, R is the size of particle, K is the dielectric constant, and $\mu = \frac{m_e m_h}{m_e + m_h}$ is effective mass of electron hole pair (exciton) in MoS_2 lattice. From these expressions, we can see that the peak of curves shown in in Figure S1D can give average size of the particle, while its width can be associated with the particle dispersion. The smaller full-width-half-maximum (FWHM) value of the NPs produced under higher applied electric field (Figure S1D) indicates narrower size distribution.

Calculation of turnover frequency (TOF)

For HER, the turnover frequency was calculated using the corresponding current density (j) and the density of active sites (N) following the expression.

$$TOF = \frac{Total\ number\ of\ H^*\ atoms\ reduced\ per\ seond}{Total\ number\ of\ active\ sites\ per\ unit\ surafce\ area} = \frac{j/2 \times q}{N}$$

Where $q = 1.6 \times 10^{-19}$ is the elemental charge and 2 shows that two H* atoms are required to produce one hydrogen molecule. To calculate TOF_{MO} per surface Mo atoms, the number density of Mo atoms (N_{Mo}) is estimated to be $\sim 1 \times 10^{15}$ per cm^2 using 3.2 A° lattice constant for MoS_2. Simplifying the expression TOF_{Mo} (s^{-1}) = 3.125×j (mA/cm^2). To calculate turnover frequency for $S\text{-}_{vacancy}$, the density of S vacancy sites in different MoS_x/NiF samples are estimated as follows:

$$N_{S\_vacancy} = 2 \times N_{Mo} \times (\%\ S\_vacancy)$$

Where % S_Vacancy is the atomic S vacancy out of the total S atoms measured by XPS (Table 1 in the manuscript). For example: $N_{S\_vacancy}$ in the MoSx/NiF@40, MoSx/NiF@ 25, and MoSx/NiF@ 10 electrocatalysts are 1.78×10^{15}, 1.55×10^{15}, and 1.21×10^{15}, respectively.

Similarly, for OER, the TOF was calculated using the corresponding anodic current density (j) and the density of active sites (N) following the expression.

$$TOF = \frac{Total\ number\ of\ O^*\ intermediate\ oxidized\ per\ seond}{Total\ number\ of\ active\ sites\ per\ unit\ surafce\ area} = \frac{j/4 \times q}{N}$$

The number 4 shows that four electrons are needed to transfer from adsorbed O* intermediate to produced one O_2 molecule.

$$TOF_{Mo}^{O_2} = \frac{j/(4 \times 1.6 \times 10^{-19})}{1 \times 10^{15}}$$

$$TOF_{S}^{O_2} = \frac{j/(4 \times 1.6 \times 10^{-19})}{N_S}$$

Where $N_S = 2 \times N_{Mo} \times (\%\ S)$. The % S is obtained from the XPS data. For example: N_S in the MoSx/NiF@40, MoSx/NiF@ 25, and MoSx/NiF@ 10 electrocatalysts are 2.2×10^{14}, 4.5×10^{14}, and 7.9×10^{14}, respectively.